U S

University of
Stavanger

Faculty of Science and Technology

MASTER'S THESIS

Study program/ Specialization: Konstruksjoner og Materialer - Maskinkonstruksjoner	Spring semester, 2015 Open access
Writer: Eivind Petersen-Øverleir	 …………………………………………… (Writer's signature)

Faculty supervisor: Vidar Hansen
External supervisor: Atle Sjølyst-Kverneland

Thesis title: "Effect of 3D printing on the Microstructure and Mechanical Properties of an Inconel 718 Nickel-alloy (UNS N07718)."

Credits (ECTS): 30

Key words: *Inconel 718* *Additive Manufacturing* *Mechanical Properties* *Microscopy* *Crystallographic Orientations*	 Pages: 79 + enclosure: 7 Stavanger, 15.06.2015

Abstract

Flow measuring instruments are important for the oil and gas industry. These instruments are exposed to hostile environments during operation. These hostile environments demands high quality materials with excellent properties, such as superalloys. Inconel 718 is a superalloy which can be manufactured by additive manufacturing. Additive manufacturing is three-dimensional printing of metals. The technology uses laser or electron beam to melt thin layers of powder material. The method allows manufacturing of complex shapes that are hard or impossible to manufacture with conventional methods. The objective of this thesis is to investigate how the additive manufacturing process affects the microstructure and mechanical properties of an additive manufactured Inconel 718 superalloy.

Additive manufacturing produces useful mechanical properties. However, yield and tensile strength is considerably lower than for commercially produced material. Therefore, heat treatments are necessary to obtain the mechanical properties achievable by the alloy composition. The heat treatment conducted in this experiment provided hardness values and tensile properties exceeding those of commercially produced material. However, this was at the cost of properties associated with ductility, elongation at break and contraction at fracture. These properties were considerably reduced and comparatively lower than with commercially produced material.

Tensile tests show that the building direction of the additive manufactured material in the as-printed condition parallel to the pull direction of the tensile test, horizontally built, is stronger than the building direction normal to the pull direction, vertically built. EBSD analysis of the additive manufactured material in the as-printed condition shows grain size differences in the various planes of the specimens. Grains are smaller in the direction of laser motion than in the direction normal to it. This means that the horizontally built material has smaller grains than the other building directions in the pull direction. This is believed to be the main contribution to the tensile property differences. The EBSD analysis also shows tendencies of grains orientating in specific directions. The additive manufactured specimen in the as-printed condition built horizontally seems to have grains orientating in preferred directions, while the vertically built seem to have grains randomly orientated, with no preferred direction. This may also contribute to the differences in tensile properties of the various build directions.

Acknowledgement

I want to express my gratitude to Professor Vidar Hansen, my faculty supervisor, for his guidance and contributions to this thesis.

I would also like to express my appreciation to Atle Sjølyst-Kverneland, my external supervisor. I am really grateful for all help you have given me.

Ingunn Cecilie Oddsen has helped me out with the scanning electron microscopy. Thank you for your guidance and contributions.

I would like to thank Roxar for providing me material for examination, office space and for allowing Atle to spend time on helping me out.

Thanks to my sister for English lessons.

I am grateful for all help given me.

Table of Contents

List of Figures

vii

List of Tables

List of Abbreviations

As-printed	The condition of a material after the printing process
ASTM	American Society for Testing and Materials
CCD	Charge-Coupled Device
CGDS	Columnar Grain Directionally Solidified
DMLS	Direct Metal Laser Sintering
EBSD	Electron Backscatter Diffraction
EBSDP	Electron Backscatter Diffraction Pattern
EBSP	Electron Backscatter Pattern
EDX	Energy-dispersive X-ray
Eosint	Manufacturer of DMLS-based 3D-printer
FE-SEM	Field Emission-Scanning Electron Microscope
HAZ	Heat affected zone
OM	Orientation Map
PMI	Positive Material Identification
SAC	Strain Age Cracking
SCDS	Single-crystal directionally solidified
SEM	Scanning Electron Microscope
SLM	Selective Laser Melting
TEM	Transmission Electron Microscope
fcc	Face Centered Cubic
bct	Body Centered Tetragonal
tcp	Topologically Close Packed
hcp	Hexagonal Close Packed

1 Introduction

Flow measuring instruments are important for the oil and gas industry's ability to control processes and ensure safety. These instruments are used down-hole in wells, subsea and on fixed and floating installations topside. Measuring instruments are exposed to high-pressure well streams that can alternate between high and low temperatures, contain sand and other abrasive particles and corrosive chemicals such as H_2S and CO_2 gas. The hostile environment therefore demands high quality materials with excellent properties. International industry standards as well as customers have strict requirements for the materials. In certain cases, alloys known as "superalloys" are needed. Superalloys are precipitation-strengthened alloys that retain remarkably high strength and corrosion resistance at elevated temperatures [1].

Conventional manufacturing processes of metals are limited by metal cutting machines, which give restricted design possibilities. Moreover, conventional machining of end products produces significant amounts of spilled material, is time consuming and cost ineffective. In addition, numerous cutting chips are consumed in the process.

Methods for manufacturing and processing of metals are evolving. A modern process of manufacturing that has been given much attention lately is additive manufacturing, which is three-dimensional printing of metals. The technology uses laser or electron beam to melt thin layers of powder material. It produces solid parts almost without the need of post processing. The method allows manufacturing of complex shapes that are hard or even impossible to produce with conventional methods. It also reduces the time it takes to manufacture, with hands-on models being produced within hours.

The objective of this thesis is to investigate how the additive manufacturing process affects the microstructure and mechanical properties of an additive manufactured superalloy. The superalloy investigated is an Inconel 718 nickel-alloy (UNS N07718). The as-printed condition and post-print heat treatments are compared to a forged bar of Inconel 718 which is solution annealed and age hardened.

2 Theory

2.1 Development of Nickel-Base Alloys

The trends of chemical composition of nickel-base alloys with time are illustrated in Figure 2.1. As compositions can be very complex, one should read the figure as a broad identification of qualitative trends. The figure does not show exact chemical content [2].
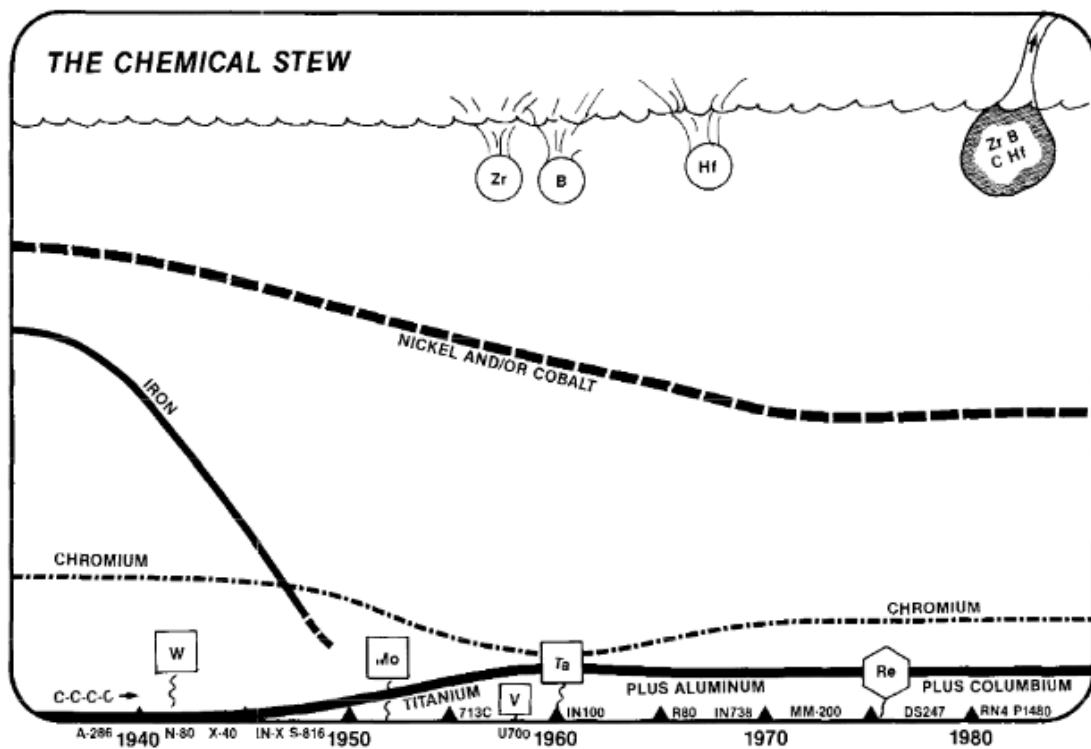
Figure 2.1: Comparative qualitative view of trends in Ni-base alloy composition (y-axis) over time (x-axis). Note that composition values are not given. The figure illustrates the varying quantity and introduction of elements over time [2].

Nickel (Ni) or iron (Fe) base with sufficient amounts of chromium (Cr) for oxidation resistance were the only alloying elements of the alloys in the early years. Small amounts of titanium (Ti), aluminum (Al) and/or niobium (Nb)(formerly columbium) were added later on. These alloying elements gave the material the coherent phase of gamma prime (γ') which provide creep-resistant. Ti, Al and Nb have never been present in large amounts as they significantly embrittle the alloy if added excessively. The most vital element of the creep-resistant phase, γ', formers is Al as it is the primary γ' former and is an important oxidation-resistant element.

Fe, emanating as a base from stainless steel, generally disappeared in favor of cobalt (Co) and Ni in the 1930s. Refractory (a material that retains its strength at high temperatures) metal additions, led by molybdenum (Mo), was found to create significant additional strength through solid solution and carbide effects in the late 1940s. Tantalum (Ta), tungsten (W) and rhenium (Re) are also utilized today [2].

To provide corrosion resistance, superalloys have fairly high levels of Cr. In the early years of cast superalloys, the amount of Cr was high. The Cr content has over the years been significantly reduced in order to accommodate other alloying elements that increase the elevated temperature strength. The Al content of Ni based alloys increased as Cr decreased [3]. In the 1960s, Cr was recognized to decrease the strength. However, the decrease of Cr introduced problems with "hot corrosion" resulting in a more careful use of the alloying element.

Carbon has always been present for solid state reactions. Carbides that precipitate acts as a point strengthener. Carbides also (and zirconium (Zr) and boron (B)) have positive effects on grain boundaries as they prevent re-crystalizing. However, these elements are not needed in the latest development of single crystal alloys as there are no phase grain boundaries.

Greater and greater amounts of differing elements have been added for specific chemical and mechanical effects over the years. Some elements were removed as advanced process developments in the 1980s created new compositions that did not require them anymore [2].

2.2   Nickel-Base Alloys

Ni-base alloys are used in a wide range of applications and environments. This makes the alloy one of the most important classes of engineering materials. The Ni-base alloys are selected for applications in need of high strength at both high and ambient temperatures, specific electrical properties, corrosion resistance at high temperatures and in aqueous environments, in addition to many other physical property-dependent applications.

The matrix of Ni-base alloys remains austenitic in solid solution from solidification to absolute zero. This means that the alloys can be used at both elevated temperatures and cryogenic temperatures. However, mechanical properties may be impaired by precipitation of e.g. σ-phase if the alloy is exposed to elevated temperatures over time. The Ni-base alloys provides useful corrosion resistance [1].

2.2.1 Classification

The classification system of Ni-base alloys is not systematic, as opposed to Al alloys and steels. Ni-base alloys are known by their trade names or by the alloy number that the producer originally assigned [1]. The various types of Ni alloys are showed below in Figure 2.2.

```
                    ┌─────────────────────────────────┐
                    │   Nickel and Nickel-base Alloys  │
                    └─────────────────────────────────┘

┌──────────────┐   ┌──────────────┐   ┌───────────────────────┐   ┌──────────────┐
│ Commercially │   │Solid-Solution│   │Precipitation          │   │   Speciality │
│     Pure     │   │ Strengthened │   │ Strengthened          │   │     Alloys   │
└──────────────┘   └──────────────┘   └───────────────────────┘   └──────────────┘

      ┌────┐           ┌────────┐            ┌────────┐                ┌──────────────┐
      │ Ni │           │ Ni-Cu  │            │Ni-Al-Ti│                │    Ni-Al     │
      └────┘           └────────┘            └────────┘                │ Intermetallics│
                       ┌────────┐            ┌──────────┐              └──────────────┘
                       │ Ni-Mo  │            │Ni-Cu-Al-Ti│
                       └────────┘            └──────────┘             ┌──────────────┐
                       ┌────────┐            ┌──────────┐             │    Oxide     │
                       │ Ni-Fe  │            │Ni-Cr-Al-Ti│            │  Dispersion  │
                       └────────┘            └──────────┘             │ Strengthened │
                       ┌────────┐            ┌────────┐               └──────────────┘
                       │Ni-Cr-Fe│            │Ni-Cr-Nb│
                       └────────┘            └────────┘
                       ┌──────────┐          ┌──────────────┐
                       │Ni-Cr-Mo-W│          │Ni-Fe-Cr-Nb-Al-Ti│
                       └──────────┘          └──────────────┘
                       ┌──────────┐
                       │Ni-Fe-Cr-Mo│
                       └──────────┘
                       ┌──────────┐
                       │Ni-Cr-Co-Mo│
                       └──────────┘
```
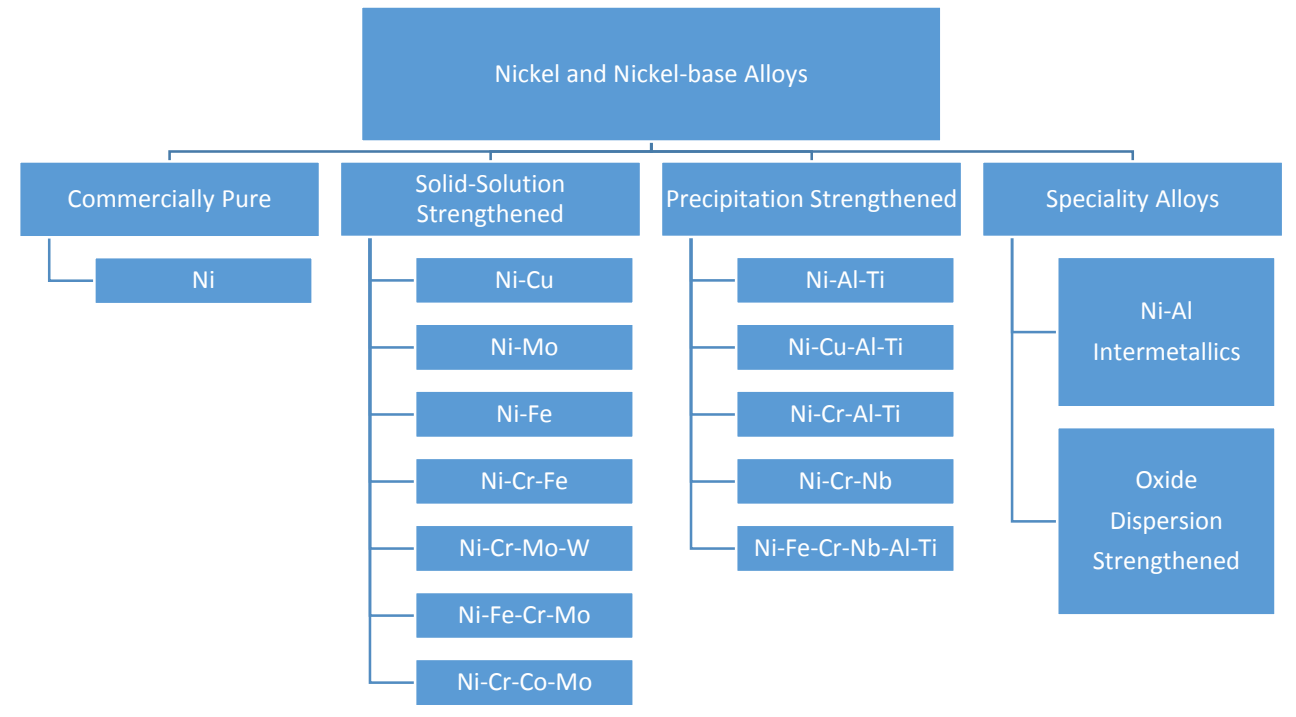
Figure 2.2: The various types of Ni- alloys [1]

2.2.2 Precipitation-Strengthened Nickel-Base Alloys

Precipitation-strengthened Ni-base alloys contain additions of Al, Ti and/or Nb. If heat-treated appropriately, these alloying elements form a strengthening precipitate with Ni. These precipitates are coherent with the austenite (γ) matrix under most conditions. The matrix are thus strained such that the strength of the alloy increases substantially. γ' (Ni_3Al, Ni_3Ti and $Ni_3(Ti, Al)$), and gamma double prime (γ'') (Ni_3Nb), are the most common of these precipitates. Precipitation-strengthened Ni-base alloys can increase strength to reach ultimate tensile strength values exceeding 1380 MPa with 0.2% offset yield strengths over 1035 MPa by optimizing alloying additions and heat treatment. In comparison, solid solution

4

strengthened alloys holds maximum ultimate tensile strength of 830 MPa with yield strength in the range 345 – 480 MPa.

Inconel 718 provides outstanding design opportunities. Excellent fatigue life at service temperatures up to 760°C is achieved when properly designed and melted. Proper melting is important to obtain low levels of impurities. The name superalloy, which Inconel 718 and other γ' and γ'' precipitation-strengthened Ni alloys are often referred to as, is well suited as these alloys retain remarkably high strength and corrosion resistance at elevated temperatures [1].

2.3 Metallurgy

The microstructure of superalloys consists of austenitic face centered cubic (fcc) matrix phase γ plus various secondary phases. Ni-base superalloys may contain a variety of secondary phases that may affect the mechanical properties of the material:

- γ': fcc ordered $Ni_3(Al,Ti)$
- γ'': bct ordered Ni_3Nb
- Carbides: fcc ordered MC, $M_{23}c_6$, M_6C and M_7C_3 (rare)
- Eta (η): hexagonal ordered Ni_3Ti
- Delta (δ): orthorhombic ordered Ni_3Nb intermetallic compounds

The unique characteristics of superalloys are given by the production and control of the strengthening phases in addition to morphology and grain size. The strength of superalloys are mostly derived from solid-solution hardening and precipitated phases. The principal strengthening precipitate phases of Ni-base superalloys are γ' and γ''. γ'' is the strengthening precipitate for Nb-strengthened Ni-base superalloys, typified by Inconel 718. For Ni-base superalloys containing Nb in addition to larger amounts of Al and/or Ti, both γ' and γ'' are strengthening precipitates. Limited strengthening may be provided by carbides, either directly through e.g. dispersion hardening, strengthening by the presence of fine particles in the lattice, or indirectly by e.g. stabilizing grain boundaries against excessive shear. The η- and δ-phases along with γ' are useful for structural control during processing of wrought superalloys. To what extent they directly contribute to strengthening depends on the alloy and its processing. In addition to solid solution hardening producing elements and elements that promote γ' and carbide formation, other elements (e.g. B) are added to enhance chemical or mechanical

properties. Some elements that form γ' and carbides may contribute significantly to enhance chemical properties as well. Phases damaging to the properties of the superalloys may also form. Laves, σ and μ are among these phases, so-called topologically close-packed (tcp) phases. However, these phases are not of concern if present only in fractions [3].

2.3.1   Chemical Composition

Alloying elements and composition for additive manufactured Ni alloy (UNS N07718) are given by ASTM F3055 – 14a standard, "Standard Specification for Additive Manufactured Ni Alloy (UNS N07718) with Powder Bed Fusion" [4] and presented in Table 2.1 below.

Table 2.1: Alloying elements and quantity range in wt% for Inconel 718, Ni alloy (UNS N07718) [4].

Element	Min	Max
Ni	50.00	55.00
Cr	17.00	21.00
Fe	Remainder	
Nb (+Ta)	4.75	5.50
Mo	2.80	3.30
Ti	0.65	1.15
Al	0.20	0.80
Co	-	1.00
Si	-	0.35
Mn	-	0.35
Cu	-	0.30
C	-	0.08
P	-	0.015
S	-	0.015
B	-	0.006

2.3.2   Brief Presentation of Nickel-Base Superalloy Precipitates

Chapter 2.3.2 is based on information provided by reference [3]. The phases are presented to give a brief understanding of Ni-base metallurgy and what precipitations to be aware of when handling and studying such material.

2.3.2.1 γ

- fcc.
- Matrix phase for all Ni-base alloys.
- Ni-base matrix phase normally contains high percentages of solid solution elements like Fe, Mo, Cr and Co.
- Non-magnetic phase.

2.3.2.2 γ'

- fcc (ordered $L1_2$). Also known as geometrically close-packed (gcp).
- Lattice parameter: 0.3561 nm for pure Ni_3Al to 0.3568 nm for $Ni_3(Al_{0,5}Ti_{0,5})$.
- Formula: Ni_3Al, $Ni_3(Al,Ti)$.
- The size of the crystal lattice varies in size from 0 to 0.5% from the γ matrix.
- The appearance of the phase varies from cubic to spherical shape. The γ' phase is in some of the older Ni-base superalloys is spherically shaped. Modern Ni-base alloys has generally a cuboidal γ' shape.
- The morphology of γ' can, shown by experiments, be changed by variations in the ratio of Al/Ti and Mo content.
- Change in shape follows the order spherical, globular, blocky, cuboidal with increasing γ/ γ' mismatch. Extended exposure of elevated temperatures, above 700°C, causes undesirable η (Ni_3Ti) phases to form when the lattice mismatch γ/ γ' is high.

2.3.2.3 η

- hcp ($D0_{24}$). Also known as geometrically close-packed (gcp).
- Lattice parameter: $a_0 = 0.5093$ nm, $c_0 = 0.8276$ nm.
- Formula: Ni_3Ti (no solubility for other elements).
- The phase can be found after extended heat exposure in Ni-base superalloys with a high ratio of Ti/Al. Before transforming to η, it may exist in a metastable form as γ' rich on Ti.
- Can form intergranularly as acicular platelets in a Widmanstätten patter. Can also form in a cellular form intergranularly.

2.3.2.4 γ''

- bct (ordered D0$_{22}$). Also known as geometrically close-packed (gcp).
- Lattice parameter: $a_0 = 0.3624$ nm, $c_0 = 0.7406$ nm.
- Formula: Ni$_3$Nb.
- It is the main strengthening phase in Inconel 718.
- The precipitates are coherent particles shaped as discs that form on the {100} planes.
- Average diameter about 60 nm.
- Thickness about 5-9 nm.

2.3.2.5 Ni$_3$Nb (δ)

- Orthorombic.
- Lattice parameter: $a_0 = 0.5106 - 0.5110$ nm, $b_0 = 0.4210 - 0.4251$ nm, $c_0 = 0.4520 - 0.4556$ nm.
- Formula: Ni$_3$Nb.
- The phase may be found in overaged Inconel 718.
- When formed between 815 - 980 ºC it has an acicular shape.
- At high aging temperatures it forms by intergranular precipitation. At low aging temperatures it forms by cellular reaction.

2.3.2.6 MC

- Cubic.
- Lattice parameter: $a_0 = 0.4300 - 0.4700$ nm
- Formula: TiC, NbC.
- M may represent Ti or Nb.
- Ti-carbide, TiC, has some solubility for nitrogen (N), Mo and zirconium.
- Variable composition.
- Appears grey to lavender as globular irregularly shaped particles.

2.3.2.7 $M_{23}C_6$

- fcc.
- Lattice parameter: $a_0 = 1.0500 - 1.0700$ nm (varies with composition).
- Formula: $Cr_{23}C_6$, $(Cr, Fe, Mo)_{23}C_6$.
- M may represent Cr, Fe or Mo.
- The shape of precipitation is important. It can precipitate as globules, lamellae, cells, films and platelets.
- It normally forms at the grain boundaries

2.3.2.8 M_6C

- fcc.
- Lattice parameter: $a_0 = 1.0850 - 1.1750$ nm.
- Formula: Fe_3Mo_3C, Fe_3Nb_3C, Nb_3Co_3C, Ta_3Co_3C.
- M may represent Fe, Mo, Nb, Co and/or Ta. Normally it is Mo.
- The carbide is randomly distributed.
- It may have a pinkish appearance.

2.3.2.9 M_7C_3

- Hexagonal.
- Lattice parameter: $a_0 = 1.3980$ nm, $c_0 = 0.4523$ nm.
- Formula: Cr_7C_3
- Normally found blocky intergranularly shaped.

2.3.2.10 M_3B_2

- Tetragonal.
- Lattice parameter: $a_0 = 0.5600 – 0.6200$ nm, $c_0 = 0.3000 – 0.3300$ nm.
- Formula: Ta_3B_2, $(Mo, Ti, Cr, Ni, Fe)_3B_2$, Mo_2FeB_2.
- M may represent Ta, Mo, Ti, Ni, Fe and/or Mo.
- Found in Ni-base alloys with an amount of around 0.03% B or more.
- Borides and carbides appear similar. Unfortunately, the borides are not attacked by the preferred carbide etchants.

2.3.2.11 MN

- Cubic
- Lattice parameter: $a_0 = 0.4240$ nm.
- Formula: TiN, (Ti, Nb)N, (Ti, Nb)(C,N), NbN.
- At temperatures below the melting point, these nitrides are insoluble.
- These nitrides are easily spotted as-polished, as they are rectangular to square shaped and have an appearance ranging from orange to yellow.

2.3.2.12 μ

- Rhombohedral.
- Lattice parameter: $a_0 = 0.4750$ nm, $c_0 = 2.577$ nm
- Formula: $(Fe, Co)_7(Mo,W)_6$
- Is in general observed in alloys containing large amounts of W or Mo.
- It forms as irregular, coarse Widmanstätten platelets at high temperatures.

2.3.2.13 Laves

- Hexagonal
- Lattice parameter: a_0 =0.4750- 0.4950 nm, c_0 = 0.7700 – 0.8150 nm.
- Formula: Fe_2Nb, Fe_2Ti, Fe_2Mo, Co_2Ta, Co_2Ti. May be of other compositions than listed.
- Most common in Co-base and Fe-base superalloys.
- It normally appears as platelets after extended exposure of high-temperatures or as irregularly shaped globules, often elongated.

2.3.2.14 σ

- Tetragonal.
- Lattice parameter: a_0 =0.8800 – 0.9100 nm, c_0 =0. 4500 – 0.4800 nm.
- Formula: FeCr, FeCrMo, CrFeMoNi, CrCo, CrNiMo.
- Mostly observed in Co-base or Fe-Ni-base superalloys. Less common in Ni-base superalloys.
- Has an irregularly shaped globules appearance, often elongated.
- It forms after extended exposure of temperatures in the range 540 - 980 ºC.

2.3.3 Most Common Precipitates in Nickel-Base Superalloys

2.3.3.1 Gamma Double Prime

γ'' formation is promoted by Nb additions. γ'' has a bct crystal structure with composition Ni_3Nb and the phase is coherent with the γ matrix. γ'' is a metastable phase as seen in the TTT-diagram in Figure 2.3. Al and/or Ti are often present in small amounts in many Nb-bearing alloys, causing small amounts of γ' precipitates. However, strengthening is primarily obtained by γ'' in the Nb-bearing alloys, such as Inconel 718. The strength provided by γ'' is caused by large mismatch strains, about 3%, between the γ matrix and the precipitate. γ'' generally prevent SAC during post weld heat treatments because the phase forms in a relatively slow manner [1].

11

2.3.3.2 Gamma Prime

γ' is an intermetallic compound. Its nominal composition is Ni_3Al with Ti along with other elements dissolved in it. The phase is only stable in a small range of compositions. The phase holds remarkable properties providing high-temperature strength to Ni-base superalloys. Matrix-precipitate mismatch is connected to the change in morphology. For mismatches of 0 – 0.2 %, γ' tends to occur as spheres. For mismatches of 0.5 – 1 % it becomes cuboidal. For mismatches of above around 1.25 % it becomes platelike. γ-γ' eutectic will form in cast alloys. It may be present after heat treatment. In addition may envelopes or films of γ' form in the grain boundary around $M_{23}C_6$ precipitate or around MC precipitate that are breaking up during service operations or heat treatment [3].

2.3.3.3 Delta-phase (δ)

δ-precipitate of the same Ni_3Nb composition as γ'' may form under certain temperature and time conditions or if Fe is absent. As seen in the time-temperature-transformation (TTT) diagram in Figure 2.3, γ'' is a metastable phase and may turn into δ-phase. δ-precipitate is always incoherent with the γ matrix and does not provide strength when large amounts are present [3]. Reduction in creep resistance and ductility is associated with the phase transition [1]. Small amounts can however be used to control and refine grain size which may lead to improved tensile properties, creep rupture ductility and fatigue resistance. Heat treatments need to be executed carefully in order to avoid precipitation of δ [3]. The risk of δ-precipitation limits alloys to a service temperature of about 650°C. δ-phase has a characteristic needle-shaped morphology, as seen in Figure 2.4 [1].
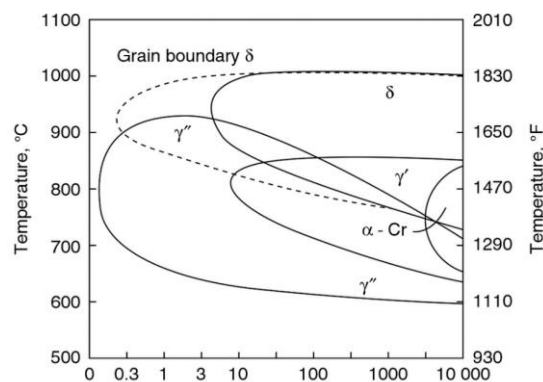
Figure 2.3: TTT-diagram for Inconel 718 Ni alloy [1]. X-axis: hours.

12
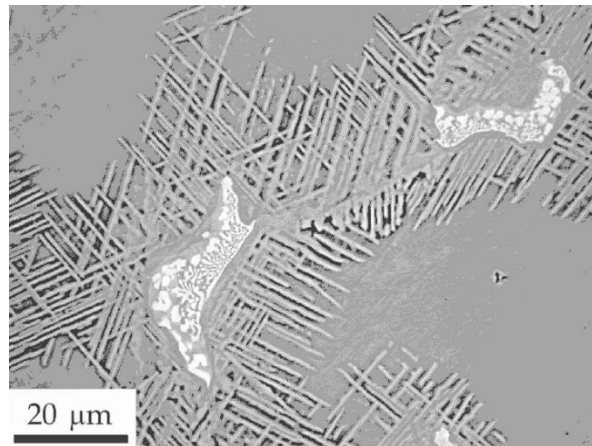
Figure 2.4: Needle shaped δ-phase surrounding Laves phase [1].

2.3.3.4 Laves

Laves phase is a hexagonal crystal structured intermetallic compound. Its chemical composition is an A_2B stoichiometry where "A" may represent Ni, Cr and Fe and "B" may represent Nb, Mo, Ti and Si. Nb and to some extent Mo partition strongly to the Laves phase formation, while the elements Ni, Fe, Cr and Ti do not partition strongly. Laves phase is well known to be promoted at the cost of the Ni_3Nb phase by addition of Fe to Nb-bearing alloys.

Addition of Si gives a similar effect. The γ/Leaves content will at a given matrix composition increase with increased content of Si. Laves phase is commonly present in Ni-base alloys because of strong segregation of Nb during solidification [1]. Laves phase precipitation is presented in Figure 2.5 below.
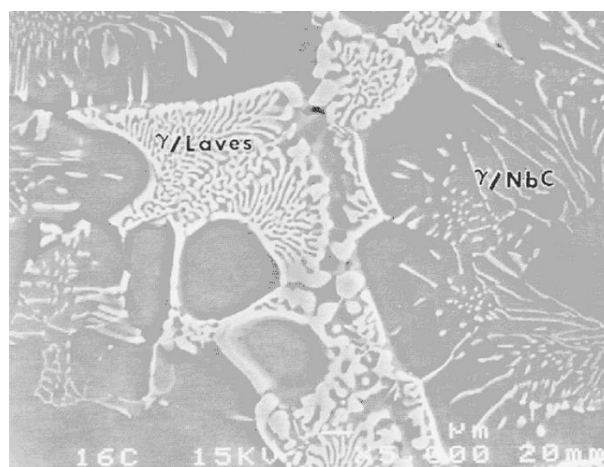
Figure 2.5: Precipitation of eutectic Laves phase and eutectic MC (NbC) carbide [1].

13

2.3.3.5 Carbides

Various types of carbides may form in Ni-base alloys with noticeable amounts of C. Most Nb-bearing superalloys contain sufficient amounts of C to promote formation of carbides and intermetallics at the end of solidification. The formation of carbides depends on the alloys chemical composition, processing route and history of service.

MC carbide formation is caused by the alloying elements Nb, Mo, Ti and Ta. The crystal structure of MC-type carbides is fcc crystal structure. The formation of MC-type carbides normally takes place at the end of solidification in a eutectic-type reaction with the γ matrix. Strong segregation of C and some metallic elements, in particular Nb, to the liquid during solidification promote the eutectic-type reaction. MC carbides normally form along the interdendritic and solidification grain boundary regions, as seen in Figure 2.6. MC carbides may during high temperature service and/or thermal processing be replaced by M_6C and $M_{23}C_6$ carbides.

$M_{23}C_6$ carbides form in the range of 760 - 980°C and are usually rich in Cr. Mo may also promote formation of the carbides. These carbides have a complex cubic crystal structure and generally forms on grain boundaries. $M_{23}C_6$ carbides can improve creep strength when present as discrete particles by restricting sliding of grain boundaries.

M_6C carbides form in the range of 815 - 980°C. M_6C carbides have like $M_{23}C_6$ carbides a complex cubic crystal structure. M_6C carbides generally form when the amount of Mo is in the range 6 - 8at% or greater [1].
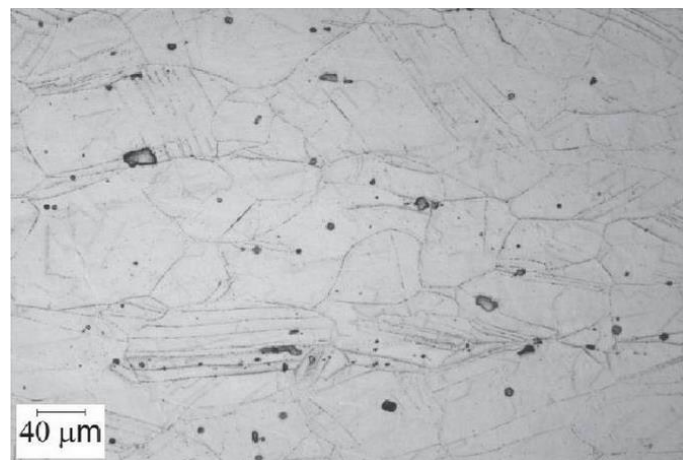
Figure 2.6: Carbide precipitation [1].

14

2.4   Strengthening by Precipitation

Precipitates strengthen an alloy by dislocation mechanisms obstructing the deformation taking place under load.

Some of the characteristics of the principle hardening precipitates that obstruct deformation are:

- The level of mismatch between matrix and precipitate. It is optimal to have the same crystal structure and about the same size of lattice for the precipitate and matrix. Hence, it is possible to pack more precipitates in the gamma matrix. For Ni-base superalloys mismatch may be up to 1 %.
- The order of the precipitates. Preferred ordering for individual atoms are introduced, as seen in Figure 2.7. Hence, the energy level required to pass deformation elements, known as dislocations, through a precipitate increases. Extra energy related to ordered atom positions compared to random or normal disordered positions are represented by an energy (antiphase domain boundary or APB) possessed by the ordered precipitates. High APB energy require large force for deformation to happen.
- The size of the precipitates. Dislocations may pass too easily through the crystal if the precipitate is too small. However, strength may be lowered and dislocations will bow if the precipitate is too big. Optimal size is dependent on the measured property. For creep rupture resistance is a single size desired. This is unfortunately only possible in specially processed columnar grain directionally solidified (CGDS) or single-crystal directionally solidified (SCDS) Ni-base superalloys. To minimize tendencies to notch sensitivity is a two-size precipitate structure desired for wrought superalloys. Higher tensile strengths may be promoted at the cost of reduced creep rupture capacity by a single size of γ' produced at low aging temperature after an incomplete solution of γ'.

If more than one element is present in a crystal structure, given elements occupy specific positions in the crystal. An example is when a secondary phase, such as Ni_3Al with fcc crystal structure, is present in a material. The Ni atoms will be placed at the face positions while the Al atoms will be placed at the corners as seen in Figure 2.7 [3].
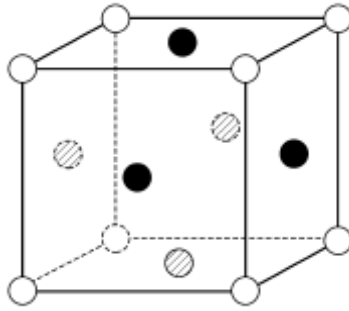
Figure 2.7: fcc crystal structure. Given elements are occupying specific positions in the crystal [3].

2.4.1 Solid Solution Strengthening

Individual alloying element atoms may dissolve into the main materials crystal structure. Atoms may dissolve substitutionally or interstitially as seen in Figure 2.8. It is called a substitutional defect when an atom takes the place of a normal atom. If the substitutional atom is smaller than the main atoms, the crystal lattice is put into tension. If the substitutional atom is larger than the main atoms, the crystal lattice is put into compression. It is called an interstitial defect when atoms much smaller than the main atoms puts itself between the lattice points. Both substitutionally and interstitially defects create stresses in the crystal lattice. The stresses works as pinning points which limits the dislocation motion resulting in a strengthened material [13].
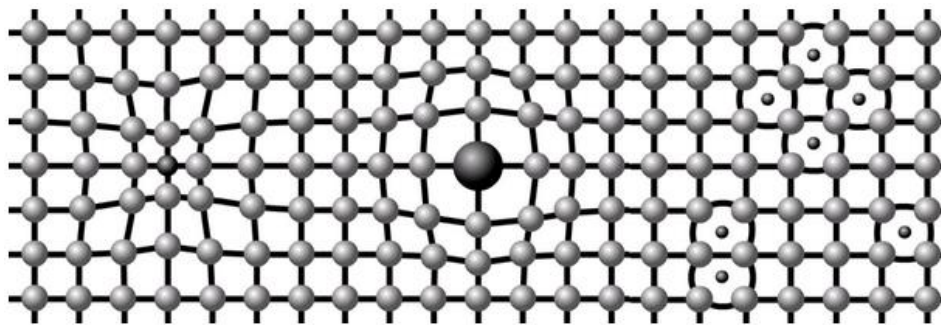
Figure 2.8: Interstitial and substitutional strengthening. Substitutional strengthening by tension to the left, substitutional strengthening by compression in the middle. Interstitial strengthening to the right [13].

16

2.4.2   Precipitation Hardening

Uniformly spread extremely small secondary phase particles that form within the original phase matrix may improve the strength and hardness properties. These precipitates prevent dislocation movement by acting as obstacles [14].

Precipitation hardening is a stepwise process as illustrated in Figure 2.9.
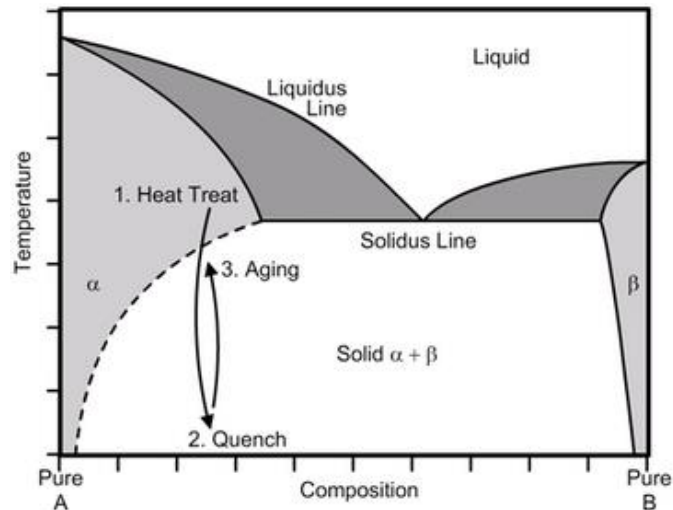
Figure 2.9: Phase diagram of arbitrary material showing the three steps of the age hardening process [13].

The steps are:

1. Heat treat the material in the temperature range were β atoms fully dissolve into the main materials crystal structure which is α in this example, above the dashed line and below the melting temperature (liquid) in the diagram. Fully dissolving β atoms result in evenly distribution of the element throughout the crystal structure of the alloy, as seen in FIGURE. Voids (empty space where an atom normally is expected) are also a result because of the thermal activity of the crystal lattice.
2. Quench the material so that the temperature drops below the atoms mobility point. By doing so, the structure is locked at the same structure as in section 1 above.
3. Heat treat the material with a temperature just below the dashed line. This is called aging. The elevated temperature allows the β atoms to come out of solid solution and gather together. The material may need to be exposed to the elevated temperature for

17

several hours to obtain this. Small islands of β atoms will be found inside the grains of α when the aging process is finished, as seen in Figure 2.10 [13].
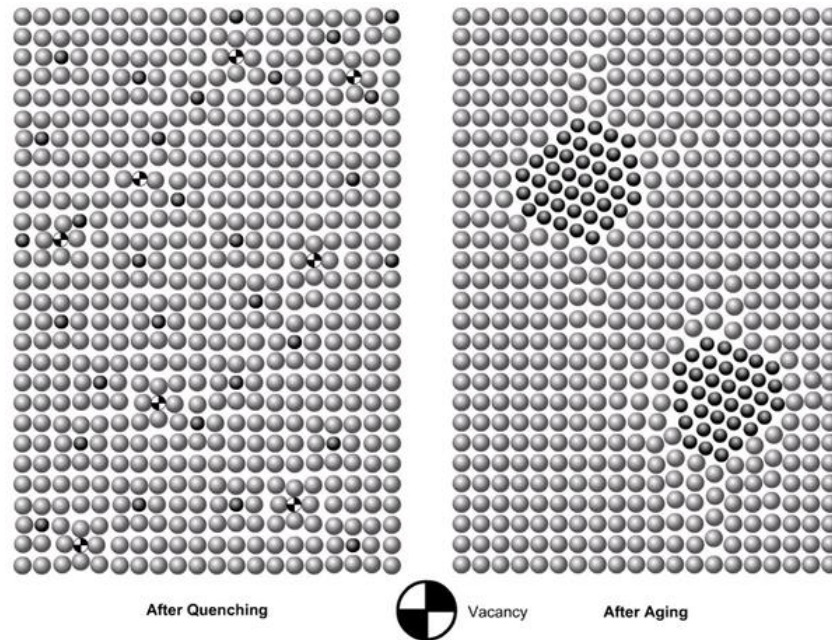
Figure 2.10: Fully dissolved β atoms and voids in the main materials crystal structure to the left. Islands of β atoms inside the grains of α to the right [13].

2.4.3   Grain Size Influence

Mechanical properties of polycrystalline metal are influenced by grain size. Adjacent grains share a grain boundary and they usually have different crystallographic orientations. Slip or dislocation motion during plastic deformation must occur across the shared grain boundary. The shared grain boundary works as dislocation motion barrier. There are two reasons for this:

- A dislocation passing a grain boundary will have to change its motion direction as the grains have different crystallographic orientations.
- The grain boundary region exhibit atomic disorder. This result in a discontinuity of slip planes between two grains.

Small grains impends dislocation motion to a greater extent than large grains, as small grains has a greater total area of grain boundaries. Fine-grained materials are therefore harder and stronger than coarse grained materials. Hall-Petch equation states that yield strength varies

with grain size according to: $\sigma_y = \sigma_0 + k_y d^{-1/2}$, where σ_y is the yield strength, σ_0 and k_y are material constants and d is the average grain diameter [15].

2.4.4   Property Achievement

A combination of cast/wrought processing followed by a suitable heat treatment usually develop the properties of a superalloy for a given composition. The chemical composition provides the level of strength and the corrosion properties. However, the key to achieving optimal properties are the processing steps. Processing develops the grain structure. Microstructural changes are without exception produced by dissolving carbides and other intermetallic precipitate phases (e.g. σ or γ') followed by causing redistribution in an appropriate form. Some of the elements mentioned above produce easily noticeable changes in the microstructure, while other elements produce discrete changes. Heat treatment and processing influences the precise microstructural effects produced. Precipitation of gcp phases like γ', carbide formation and formation of tcp phases like σ are the most apparent effects on the microstructure [3].

2.5   Solidification

Inconel 718 contain relatively large amounts of Nb to strengthen the alloy by formation of the γ'' phase. Solidification of commercial Nb-bearing alloys is a three step solidification process for most of the alloys, as seen in Figure 2.11. The primary solidification stage L → γ is followed by L → γ + NbC and last L → γ + Laves. Note that the C content of the alloy is of importance to these reactions. Large amounts of C may completely suppress the formation of the lower temperature reaction L → γ + Laves as this reaction always occur after the L → γ + NbC reaction. The L → γ + NbC reaction may not occur at all if the C content is very low. Eutectic-type structures like NbC and Laves are highly enriched in Nb. Hence, an increase in Nb content promote higher volume fractions of total eutectic. The amount of γ/NbC and γ/Leaves constituents will increase by additions of Nb to an alloy containing large amounts of Fe and C.

The melting point of Fe is higher than for Ni. Solidification of Fe will therefore occur before Ni and higher reaction temperatures of Fe is expected. Nb and C segregates strongly during solidification. The segregation potential of Nb is increased by Fe. This leads to an increase of

secondary phase formation, as both secondary phases NbC and Laves that form during solidification is Nb rich. γ-Ni can dissolve a maximum of 18.2wt% (at 1286°C) while γ-Fe can dissolve as little as 1.5wt% Nb (at 1210°C). An increase in Fe thus lead to a decrease in solubility of Nb in the γ-matrix (Ni, Fe, Cr) [1].
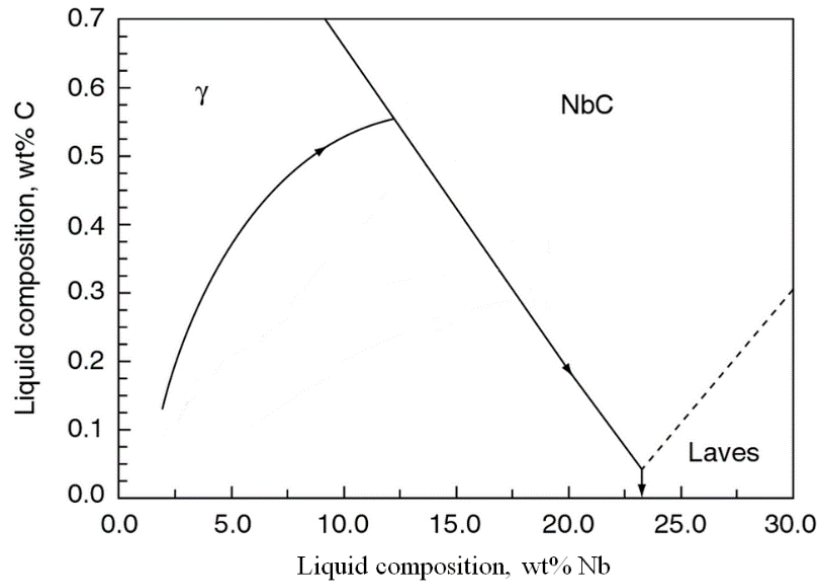
Figure 2.11: Solidification process for Nb-bearing alloys [1].

2.5.1   Reaction Sequence of Nb-bearing Superalloy Solidification

The first step of the solidification process is formation of γ dendrites, L → γ. γ dendrites reject Nb and C to the liquid upon solidification. As solidification of γ dendrites proceed, the remaining liquid progressively become richer in Nb and C. This continues until the solidification process reaches the eutectic line between γ and NbC. γ and NbC form from the liquid simultaneously by an eutectic-type reaction, L → γ + NbC, at this point. From here on, the liquid composition moves down the eutectic line until the element C is depleted by γ/NbC solidification. The solidification process should according to solidification modeling end with the ternary eutectic reaction L → γ + NbC + Laves, but an intermix of these three is not observed in alloys forming both Laves and NbC. However, the process ends with the L → γ + Laves eutectic reaction when the liquid contains about 19.1wt% Nb and 0.03wt% C. γ/NbC and γ/Laves constituents are consistently clearly separated [1].

20

2.5.2   Solidification Cracking

Cracking upon solidification of welds is a function of Nb added as a strengthening aid to the alloy. γ/NbC and γ/Laves constituents are formed by eutectic reactions as a result of Nb segregation during solidification. These constituents raise the temperature range of solidification and promotes cracking, as seen in Figure 2.12. It may be difficult to prevent solidification cracking because the amount of Nb added is intentional for mechanical purposes. Solidification cracking may also be promoted by the presence of sulfur (S) and phosphorus (P). However, these impurity elements are normally kept at low levels and shall not exceed 0.015wt% for Inconel 718 [1].
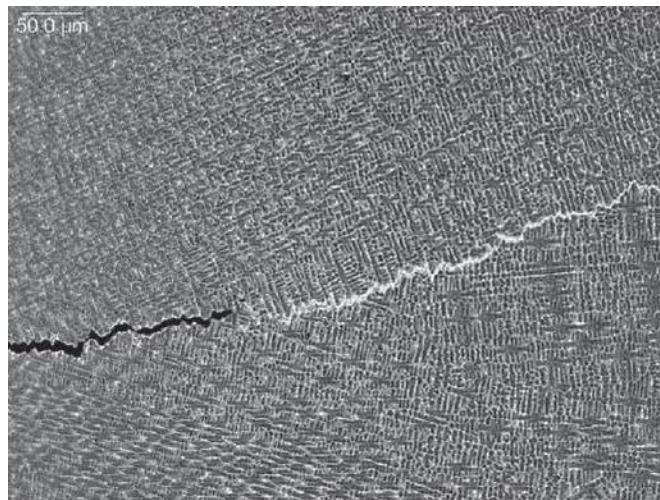
Figure 2.12: Solidification crack in Nb-bearing alloy [1].

2.6   Scanning Electron Microscope

A Scanning electron microscope (SEM) image of a sample is produced by rastering an electron beam over the sample surface. Two different types of electrons are emitted by interactions in the sample and are collected by an appropriate detector. The two types are secondary electrons and backscattered electrons. Secondary electrons is a result of inelastic collisions, while backscattered electrons are scattered elastically. A secondary electron is an electron that has been knocked out of its orbital by a primary electron from the incident beam. Inelastic collisions also cause emission of characteristic x-rays [6]. Figure 2.13 illustrates the two types of electron emission and the characteristic x-ray emission.
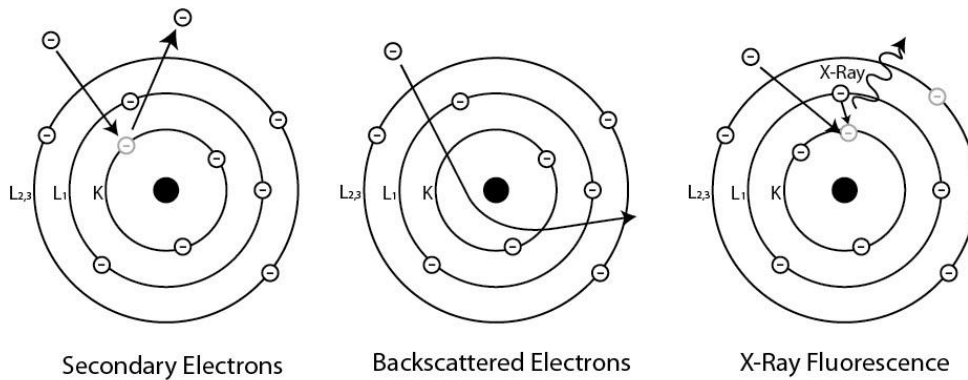
Figure 2.13: Electron interactions and x-ray emission [6].

The quantity of backscattered electrons are dependent on the atomic number. A high atomic number results in many backscattered electrons, while a low number results in few backscattered elements. Heavy elements will appear brighter than light elements in the SEM image because heavy elements produce more backscattered electrons and hence more signal. Backscattered electrons are beneficial for studying precipitates and different phases. The sample does not need to be etched to study backscattered electrons.

When an inelastic electron collision take place, characteristic x-rays are emitted from excited atoms. These x-rays may be used to quantitatively analyze individual points on a sample. All elements produces x-rays with a unique characteristic quantity of energy. Because all x-rays are unique, these can be collected and measured to qualitatively and quantitatively identify elements under the electron beam [6].

2.6.1 Diffraction

Scattering of electrons occur when the incident electron beam hit the sample surface. Electrons are scattered away from the incident beam. Both elastic and inelastic scattering processes (diffraction) occurs. Elastic scattering (Bragg-scattering) cause changes in the direction of the incident electrons, while inelastic scattering cause change in both direction and energy of the incident electrons. The inelastic scattering results in a diffused background in a diffraction image [7].

Angles for both coherent and incoherent scattering from a crystal lattice are given by" Bragg's law". Re-emitted wave fields caused by a coherent spin interaction with an unpaired

22

electron, interfere constructively or destructively with each other as a result of the wave nature motion of electrons. Overlapping waves that interfere constructively add up together and produce stronger peaks, while destructively interfering waves subtract from each other and produce weaker peaks as seen in Figure 2.14. This produces a diffraction pattern that can be seen on a film or detector. Diffraction analysis is based on the resulting wave interference pattern and is called "Bragg diffraction" [8].
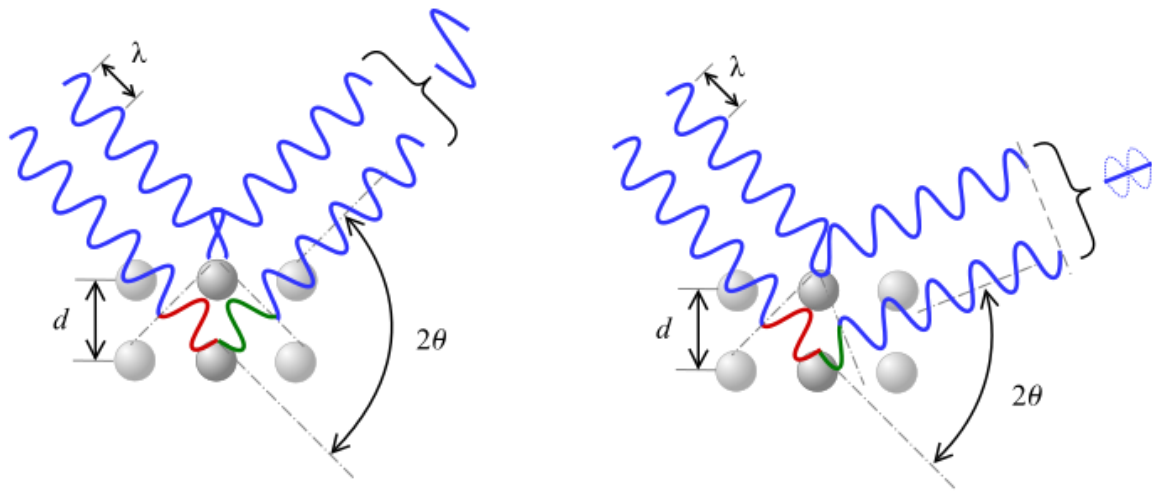
Figure 2.14: Constructive interference to the left and destructive interference to the right caused by phase shift, according to the 2θ deviation [8].

Bragg diffraction take place when radiation with wavelength similar to atomic spacing scatter in a mirror-like fashion and results in a constructive interference. The interplanar distance *d* separates the lattice planes that scatter the waves in a crystalline solid. When constructive interference occur between scattered waves, waves stay in phase because each waves path length equals an integer multiple of the wavelength as seen in Figure 2.15. Two interfering waves has a path difference given by *2dsinθ*, where θ is the scattered angle. A cumulative effect of reflection intensifies the effect of constructive and destructive interference. The effect accumulates in successive crystallographic planes in the crystal lattice. This sums up in an equation called "Bragg's law":

2dsinθ = nλ

The law determines what scattered angle, θ, which gives the strongest constructive interference. λ is the incident wavelength and n is a positive integer. One can achieve a diffraction pattern by measuring scattered waves intensity as a function of scattering angle.

Scattering angles that satisfy Bragg conditions result in very strong intensities in the diffraction pattern. These intensities are known as "Bragg peaks" [8].
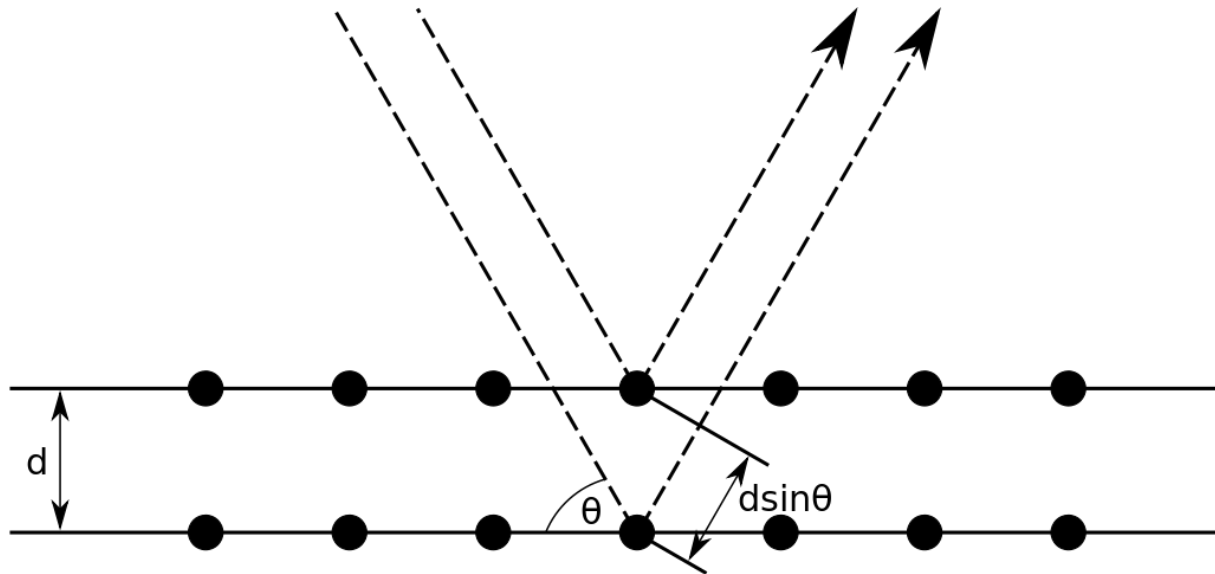
Figure 2.15: Two different atoms within a crystalline solid scatter two beams with identical wavelength and phase. The lower beam travels and extra length of 2dsinθ. When the extra traveling length is an integer multiple of the wavelength, constructive interference occurs [8].

2.6.2 Electron Backscatter Diffraction Technique

Microstructural information of the crystallographic nature of metals, semiconductors, ceramics and minerals, actually most inorganic crystalline metals, are quantitatively provided by electron backscatter diffraction (EBSD). Texture, phase identity, grains size, grain orientation and grain boundary character of the sample under the beam are reveled. Analyzes of metal thin films with nanograins, to centimeter-sized samples with millimeter-sized grains may be performed. The limit of the nominal angular resolution is ≈ 0.5 °. The spatial resolution is connected to the resolution of the SEM. However, 20 nm sized grains may be measured with modern field emission SEMs (FE-SEMs). The ability to orient a sample at 70 ° tilt at a suitable working distance, usually between $5 - 30$ mm, determines the macroscopic sample size. The orientation ability is dependent on the stage and chamber of the SEM [9].

24

2.6.2.1 How the EBSD Technique works

A flat, highly polished sample is mounted at an angle of about 20 ° to the incident electron beam as seen in Figure 2.16. Electron diffraction occurs from the point where the incident beam hit the sample surface with accelerating voltage of about $10 - 30$ kV and about $1 - 50$ nA incident beam currents [9].
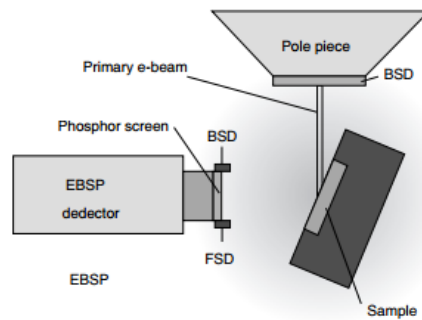
Figure 2.16: Schematic illustration of the arrangement for EBSD analysis [9].

EBSD pattern (EBSDP) emanates spherically from the point where the incident beam hit the sample surface. Backscattered electrons with low loss of energy are channeled from the crystal lattice and out of the specimen when the primary beam interacts with the lattice as seen in Figure 2.17. These low energy loss backscattered electrons are subject to path differences that lead to interference, both constructive and destructive. A diffraction pattern can be seen by the use of a phosphor screen placed in the path of the diffracted electrons at a short distance away from the tilted specimen [9].
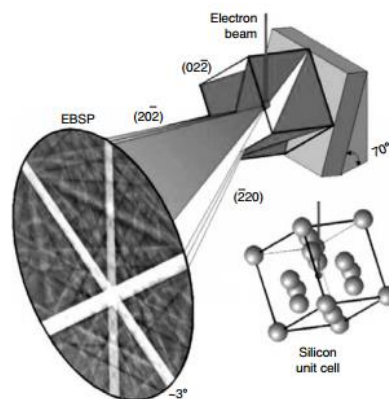
Figure 2.17: Schematic illustration of electron diffraction [9].

25

SEM electron optics governs the spatial resolution of the EBSD technique as in conventional electron backscattered techniques. High performance FE-SEMs combined with short working distances and small samples are needed if high resolution imaging of nanograins is desired [9].

2.6.2.2 Electron Backscatter Pattern

The electron backscatter pattern (EBSP) detector is connected to a free port on the SEM chamber. The port should be placed orthogonal to the tilt axis to allow the stage to tilt the sample towards the detector at about 70 °. However, it is possible with other orientations. Highly tilted samples need moderate working distances. A working distance of about 20 mm is generally allowed by the ports positioning of the detector. If the SEM port and EBSP detector allows close proximity to the objective lens, shorter working distances may be obtained for small samples. Special detectors for less convenient port positions are available.

The EBSP detector is a digital camera. The spherical diffraction pattern that emanates from the point where the incident beam hit the sample surface intersects with the phosphor screen which illuminate the Charge-Coupled Device (CCD) chip of the digital camera. The diffracted electrons are converted by the phosphor into light that is recordable for the CCD camera. EBSP is analyzed and stored by directing a stationary beam to a point on the sample. The EBSP is uniquely defined by several parameters:

- The lattice of the particular crystal under the electron beam
- The crystals orientation in space
- The electron beam's wave length, which corresponds to the accelerating voltage of the electron beam
- The EBSP detector's proximity to the sample

The EBSP is analyzed by the use of specialized computer software. It detects Kikuchi bands by the use of an optimized Hough transform. All possible orientations with each phase are determined by the software if the candidate phases under the beam are identified by the user. The software reports the best fit as the identified phase and orientation. The EBSP is considered indexed when the phase and orientation of the pattern are known [9].

2.6.2.3 External Scan Interface

Characteristic x-rays are produced when the incident electron beam hit the sample. Most SEMs are equipped with EDX (Energy-dispersive X-ray) spectrometers that determine the chemical composition by analyzing the characteristic x-rays. Modern EDX systems take control of the beam location by the use of the external scan interface existing on most SEMs. The same interface are required for EBSD. Thus a simple electronic method to share the external interface are needed for retrofitted EBSP detectors. Between the SEM and the EDX is an intelligent switch box installed, as seen in Figure 2.18. The switch box arbitrates between the EBSD and EDX systems' access to the SEM and the external scan interface. For covering large sample areas, integrated stage motion is required in addition to beam control. The integrated SEM motorized stage motion are often accessible through Ethernet connection or an RS232 serial computer interface [9].
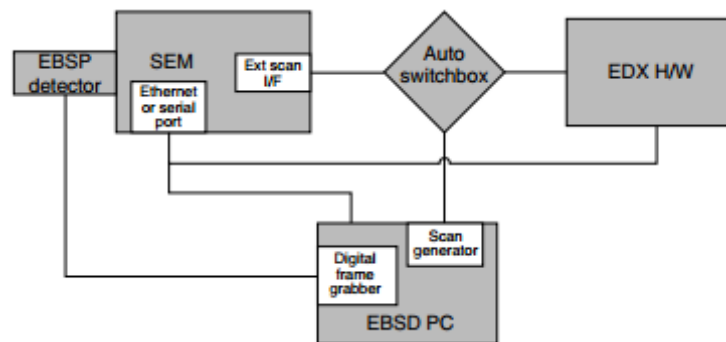
Figure 2.18: Schematic illustration of the SEM interface [9].

2.6.2.4 Orientation mapping

An orientation map (OM) is an image displaying crystal orientations. Creation of an OM has become practical as automated accuracy and overall speed developments of the technique allows the ability to scan the beam over multiple points on the sample. Creation of an OM has become the normal method for microstructural investigation with EBSD. Sampling step size between points, location and size defines the map. Thus, map resolution may be adjusted to reveal the grain boundary character and the grain structure. This depends on the size of the sample area required, electron beam resolution during sampling and the time available. Over the years, speed improvements has been made. An exponential increase in rate of change from

the beginning is approximated, from manual to 100 automatically indexed patterns per second.

A single dimensional output signal is produced by detectors used in normal SEM imaging. A signal is recorded from a given point on the sample where the beam is focused and acts as the brightness in the output image. However, EBSD produce a 3D pattern that emanate from the point where the beam is focused. The pattern is recorded in 2D on the phosphor screen. This means that a 2D image of the diffraction pattern is analyzed for every analyzed point on the sample. Consider a 512 x 512 pixel sample area is analyzed. With the use of EBSPs of 512 x 512 x 8 bit pixels in size, a total of 512^4 or 64 GB of uncompressed raw data for one map is produced. This very amount is in practice not always stored. At each point, only the orientation, position, phase and some data quality information are stored [9].

2.7   Additive Manufacturing

3D printing technology is an additive manufacturing technology, also referred to as rapid prototyping. Additive manufacturing uses a laser to melt powder metal. Many successive layers are melted on top of each other to make a physical model. Direct metal laser sintering and selective laser melting are examples on additive manufacturing techniques. Direct metal laser sintering and selective laser melting are similar techniques.

2.7.1   Direct Metal Laser Sintering Technique

Modern Direct metal laser sintering (DMLS) is a process that complements traditional machining. Fully dense metal parts are produced by DMLS, directly from CAD models. The process produce parts with accuracy and surface finish adequate in some cases to go directly into service. DMLS can produce highly complex parts that are impossible to produce by machining. Laser-based additive manufacturing processes, like DMLS and SLM, builds parts from the bottom up. DMLS uses an ytterbium (Yb) laser to melt and fuse microscopic grains of metal powder. Parts of imaginable shapes may be produced. The size of the part is restricted by the size of the build chamber that is roughly the size of a microwave oven. Five various high-strength alloys may be produced by DMLS: Aluminum, Titanium, Inconel, stainless steel and Co-chrome. The building process is illustrated in Figure 2.19. It is a stepwise manufacturing process following these steps [10]:

1. The CAD model is sliced into paper-thin layers digitally by software. Any needed support structures are designed to aid the structure.
2. The file is uploaded to the machine.
3. The powder bed is filled with powder of chosen alloy. The powder is distributed across the build platform in a thin layer.
4. The bottom layer of the part and any needed support structures are built by a high-powered laser.
5. Another thin layer of powder is scraped across the part by a rubber wiper.
6. The process is repeated
7. When the process is completed, the part is nearly finished. The part is removed from the build chamber and support structures are removed. Further the part can be processed per customer requirements [10].
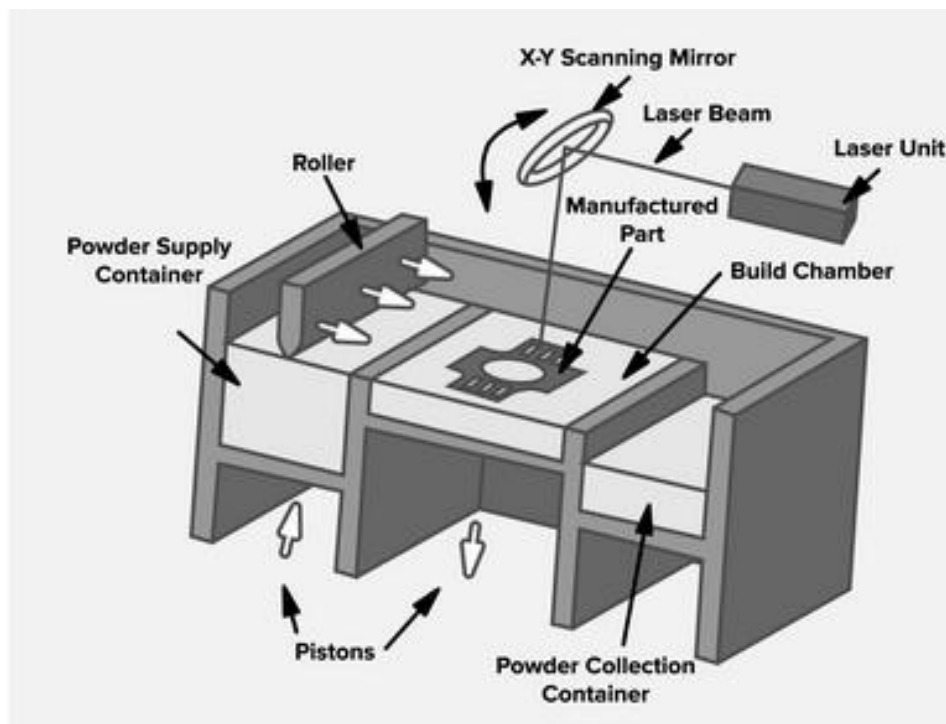
Figure 2.19: Schematic illustration of the building process in a DMLS based additive manufacturing machine [10].

2.8 Mechanical Tests

2.8.1 Tensile test

A tensile test is a test where a material is pulled until breakage. The test determines how a material reacts to forces applied in tension. Elongation and strength of the material are found and a complete tensile profile is obtained as the material is being pulled until breakage. How the material reacted to the applied forces is showed in a resulting curve as seen in Figure 2.20 [11].
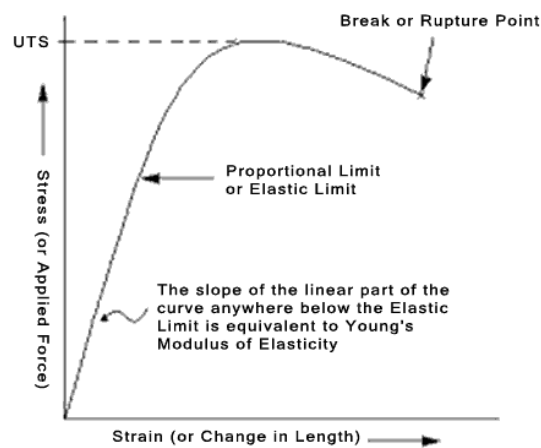
Figure 2.20: Illustration of a resulting tensile profile curve [11].

The relationship of the applied force to the elongation of the specimen is linear in the initial part of the tensile test for most materials. The relationship is defined as "Hooke's Law". The ratio of stress to strain is a constant, E, in the linear region. E is the slope of the line in the linear region as seen in Figure 2.21. It is called "Modulus of Elasticity" or "Young's Modulus". The ratio is given by the relationship: $\frac{\sigma}{\varepsilon} = E$ [11].
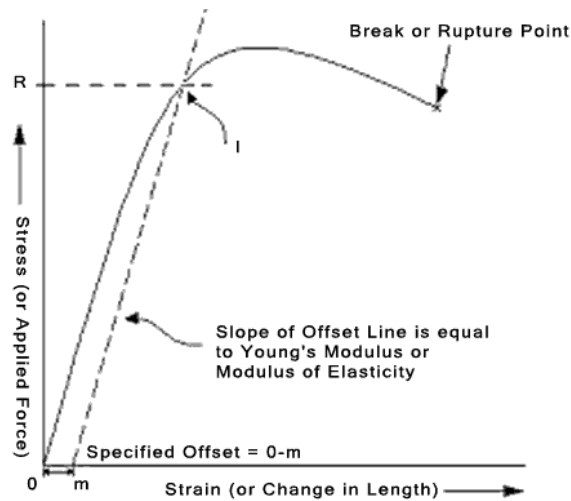
Figure 2.21: Illustration of the resulting curve showing the elastic region with an offset line equal to the modulus of elasticity [11].

The modulus of elasticity, E, only applies in the linear region of the curve. It is a measure of a materials stiffness. A load applied to a specimen within the linear region, does not plastically deform the material. The material will return to the same condition as before, when the load is removed. Plastic deformation occurs at the point where the curve is no longer linear and the linear relationship, "Hooke's Law", does not apply. This point is called the "Proportional, or Elastic Limit". From this point and further on, increase in load or stress will result in a permanent deformation. The material will no longer return to its original unstressed condition when the load is removed.

Yield strength is a value given by how much stress a material is exposed to at which plastic deformation starts to occur while loaded.

It is not always easy to define where the linear elastic region stops. As a result, an offset method to determine the yield strength is applied. The offset value is given in percentage of strain. ASTM E8 is a directive for the method and it suggests a 0.2% offset for metals. At the intersection point where the actual curve meets the offset line, which is drawn from the offset "m" and has a slope equal to the modulus of elasticity, the stress "R" is determined. This value gives the yield strength by the offset method.

An absolute measurement can express the amount of elongation or stretch a specimen undergoes during tensile testing. A change in length or a relative measurement called "strain" can express the stretch or elongation. There are two different ways to express strain. It can be

31

expressed as "engineering strain" and as "true strain". The change in length to the original length defines "engineering strain", while "true strain" is based on the instantaneous length of the specimen while the test is in progress [11].

Engineering strain: $\varepsilon = \dfrac{L-L_0}{L_0} = \dfrac{\Delta L}{L_0}$

True strain: $\varepsilon = \ln\left(\dfrac{L_i}{L_0}\right)$ where L_i is the instantaneous length and L_0 the initial length.

Ultimate tensile strength is the maximum load a specimen sustains during a test. UTS does not necessarily need to be equal to the strength at break. It is dependent on material [11]. As illustrated in Figure 2.20 and Figure 2.21, strength at break usually is lower than UTS. UTS is also referred to as R_m, tensile strength.

A polycrystalline material is an assemblage of crystal grains of various shape and size. Properties of all individual grains affect the macroscopic properties of the polycrystalline material. Single crystal elastic deformation display anisotropy in most materials. It is dependent on the crystal orientation. Macroscopic behavior of polycrystalline material can however be considered as homogeneous and isotropic in terms of elastic deformation when the crystallographic orientations in the material are fully random, said to have no or random texture. The crystal orientation of an individual grain in a polycrystalline material has a minor influence on the elasticity. Engineering structural materials are therefore usually considered by the properties of the assemblage, such as Young's modulus (modulus of elasticity), and not by the individual grain. However, when a material consist of insufficient numbers of grains, the assumption may be untrue. Young's modulus is dependent on individual crystal grain orientation and the elasticity of a single crystal when the microstructure consist of a small number of grains. For textured materials is Young's modulus influenced by each grains crystal orientation, even when the microstructure consists of sufficient numbers of grains. Identifying crystal orientation and elasticity of each grain is important to estimate Young's modulus of a textured material. Identifying crystal orientation of each grain may be done by EBSD analysis [16].

2.8.2 Hardness

Hardness is not a fundamental physical property. However, it characterizes a material. The hardness of a material is defined as its resistance to indentation. A hardness test is performed by using a fixed force (load) on an indenter. The hardness is determined by measuring the permanent indentation in the specimen. By measuring the area or the depth of the indentation, hardness value is obtained. Thus, the bigger the indentation, the softer the material [12].

The Vickers hardness test method uses a square base shaped diamond indenter. The indentation made in a test specimen is measured and converted to a hardness value. The method is based on an optical measurement system [12].

3 Experimental

An additive manufactured Inconel 718 Ni-base superalloy have been investigated. Additive manufactured specimens were manufactured by an EOSINT M 280 additive manufacturing metal printing machine based on the DMLS technique. The additive manufactured specimens were investigated in the as-printed condition and in the post-print heat-treated condition and compared to a forged bar of Inconel 718 that were solution annealed and age hardened. Additive manufactured specimens were built in three different building directions, as shown in Figure 3.1. The building directions were horizontal, H, vertical, V and diagonal (45 degrees), D.

H   **D**   **V**
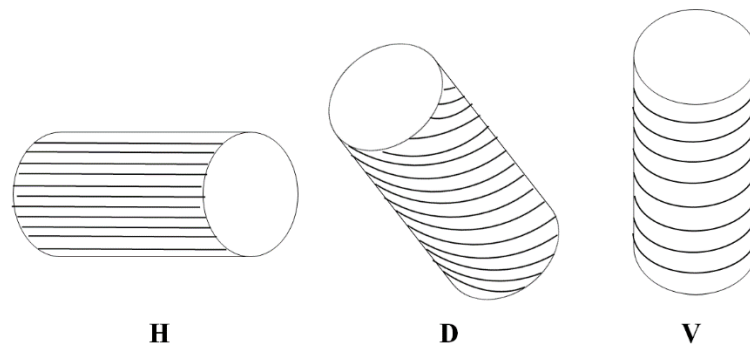
Figure 3.1: Illustration of the three different building directions.

Table 3.1: Name and condition of all test specimens.

Specimen	Condition
H P	As-printed
V P	As-printed
D P	As-printed
SH P	As-printed
H H	Solution annealed and age hardened
V H	Solution annealed and age hardened
D H	Solution annealed and age hardened
SH H	Solution annealed and age hardened
FB	Solution annealed and age hardened
FB H	Solution annealed and age hardened twice

Names and condition of all test specimens are presented in Table 3.1. Specimens in the as-printed condition are referred to as V P, H P and D P, where V, H and D refers to the building direction and P to the as-printed condition of the specimens. Specimens in the heat treated condition, solution annealed and age hardened, are referred to as V H, H H and D H, where V, H and D refers to the building direction and H to the heat treated condition of the specimens.

In addition, two specimens for tensile comparison were manufactured by an additive manufacturing metal printing machine based on the SLM technique. SLM printed specimens used for tensile tests are referred to as SH P and SH H, were S refers to SLM print, H to building direction and P and H to the as-printed and heat treated condition, respectively, of the specimens.

The forged bar reference was delivered in the solution annealed and age hardened heat treated condition. The forged bar specimen in the as-delivered solution annealed and age hardened condition is referred to as specimen FB. The forged bar specimen in the re-heated condition, solution annealing and age hardening executed in this experiment, is referred to as specimen FB H.

3.1   Heat Treatments

Heat treatments were conducted in a Nabertherm oven. The thermostat of the oven was suspected to have errors and therefore, a thermometer of type EL-EnviroPad-TC was used to control the temperature. The suspected errors were confirmed and the thermometer was used to set the correct temperature. The first heat treated specimen had thermal wires welded to it. The wires were plugged into the thermometer so that the temperature could be measured and controlled during heat treatment. The temperature was logged. Welding wires to every specimen would be an ineffective process. Thermal wires were therefore welded to a single "dummy" sample, a random piece of metal, which was used to control the temperature in the oven. The "dummy" sample had no other use than measuring the temperature. The thermal wires were pulled through the ventilation channel of the oven, so that no heat would escape through the oven door and the "dummy" sample would lay still inside the oven. Closing the door with the thermal wires between the door and the oven made the "dummy" sample move inside the oven because of the stiffness of the thermal wires and the low weight of the "dummy" sample. This could lead to the "dummy" sample touching the heating elements in

the oven or making the "dummy" sample touching the specimens used in the experiment. All heat treatments were logged. Heat treatments were performed as follows:

- Solution annealing: 2 hours, 1025 °C, water quench
- Age hardening: 8 hours, 775 °C, air cool

One specimen in each build direction and one specimen of the forged bar was heat treated. This heat treatment was chosen because the very same heat treatment was performed on the forged bar reference material according to the data certification for the material. This heat treatment is according to Special Metals Society [17] a special heat treatment for use in oil filed applications. Heat treatment of the Forged bar specimen was conducted to make a quality assurance of the heat treatment procedure made in this experiment.

3.2 Metallographic Preparation

The cylindrical heat treated additive manufactured samples was about 25 mm long and had a diameter of about 10 mm. Tensile test specimen were heat treated in the shape they had when pulled apart during tensile testing. The reference material was delivered as a 100 mm long bar with diameter of about 25 mm. A Struers Discotom-5 was used to cut off a piece with size more comparable to the printed specimens for heat treatments, about 12 mm long. Large amounts of cooling liquid were used to avoid heat generation.

All specimens were wet grinded and polished by the use of a Struers Planopol Pademax-2. Grit papers in the range 80 - 4000 were stepwise used to grind the sample surfaces of all specimens starting at 80 and ending at 4000. For every time a new grit paper of finer grade was applied, the sample surface was rinsed by the use of cotton and water to remove particles torn off by the previously used paper. The sample surface was cleaned with ethanol to remove water when the wet grinding process was finished. Polishing where conducted by the use of Mol and Nap cloth for 3µm and 1 µm respectively. Struers DP-Lubricant blue was added to the cloth to lubricate while polishing. Distilled water and cotton was used after both polishing steps to rinse the sample surface. The water was removed with ethanol after both polishing steps.

Etchant used for optical light microscopy examination of all specimens was Kalling's No.2 [18]. The etchant consists of the following:

- 200 ml methanol
- 200 ml HCl
- 10 g $CuCl_2$

The etchant was applied to the sample surface with the use of a syringe. One dose of Kalling's No.2 was applied to the sample surface every 15 seconds for one minute, resulting in four doses applied. The specimen were immediately put into distilled water after etching to stop the etching process.

Etchant used for SEM examination of dendritic structure contained the following [5]:

- 10 ml HCl
- 3 ml H_2O_2

The examined specimen were immersed into the solution for ten seconds before put into distilled water immediately after etching to stop the etching process.

Mechanical preparations for microscopy may cause tension in the surface, resulting in an amorphous (no long-range regularity in its atomic structure) surface of the specimen. Atomic structure is the key for EBSD analysis and creation of orientation maps (OM). If there is no structure, there is no pattern and hence nothing to analyze. Samples for EBSD analysis were therefore electropolished after wet grinding and mechanical polishing by the use of a Struers LectroPol-5 with an etch containing the following [19]:

- 70 ml H_2O
- 200 ml glycerol (also called glycerin)
- 720 ml H_2SO_4

The following parameters were used:

- Voltage: 20V
- Flow rate: 20
- Time: 15s

The Struers LectroPol-5 automatically adjusted the electric current. Currents used were in the range 0.01 – 0.06 amperes. The etch temperature during electropolishing were 22 – 23ºC.

3.3 Microstructural Analysis

An optical light microscope of type Reichert-Jung MeF3 were used for optical analysis of the microstructure. All specimens were examined with the optical microscope. A Zeiss Supra 35 VP SEM equipped with an Ametek EDAX spectrometer and a retrofitted EBSD UF-1000 detector was used for analysis of chemical compositions, large magnification and EBSD analysis. All specimens were examined with the use of EBSD detector. Medium working distances (~20 mm) were used for EBSD analysis. Typical settings for EBSD analysis can be seen in Appendix C. EBSD scan software was of type NORDIF. SEMDiff software was used for evaluation of the scan provided by NORDIF. SEMDiff analyzes diffraction patterns (Kikuchi lines), detects crystallographic orientations and provides grain boundary images. SCOM software was used for orientation mapping based on data provided by the SEMDiff software. All SEM images were made by detection of backscattered electrons. Characteristic x-rays were detected for chemical composition analysis. Microstructural analysis of all samples in both microscopes were made from the x-plane, as seen in Figure 3.2.
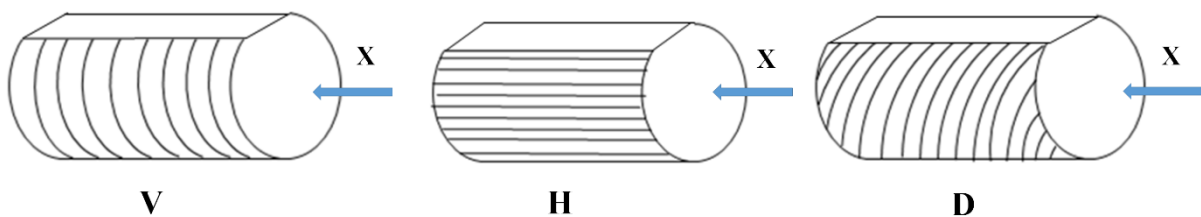
Figure 3.2: Illustration of examined plane for all specimen.

3.4 Tensile Tests

Tensile tests were performed in a machine of unknown type by Applus, located at Bryne, Rogaland. The test specimens were machined by a cnc machine of unknown type. Dimensions of the round cross sectioned test specimens were: gauge length 25 mm, diameter 5 mm.

Eight tensile tests were performed. One sample of every build direction in the as-printed condition and one sample of every build direction in the post-print heat treated condition as seen in Figure 3.3 were tested. Additionally, two samples of commercially produced Inconel

718 in the as delivered condition were tested. No re-heat treated forged bar specimen was tested.
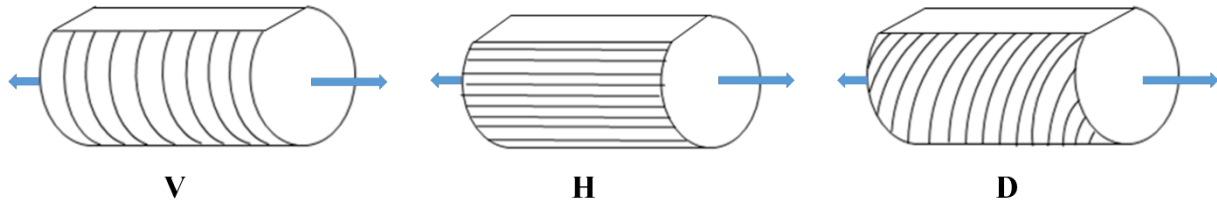
Figure 3.3: Illustration of building directions and how they were pulled apart.

An extensometer was attached to the specimens during load to measure changes in length of the specimens. The extensometer was removed when plastic deformation of the specimens started to occur. The extensometer was applied to determine the modulus of elasticity of the specimens.

3.5 Hardness Tests

Hardness tests were performed in a Struers DuraScan Vickers hardness testing machine. HV10 (10kg) was used as test force because the material is relatively hard and this was the largest force possible on the machine. The distance between each indentation was at least three times the mean diagonal of the indentations, in order to avoid areas that may have been hardened because of deformation caused by another indentation. The distance from the edge of the specimen to all indentations was at least three times the mean diagonal of the indentations, which should be sufficiently far away from areas that may contain tensions from the manufacturing process. Eight indentations were randomly made in every specimen, except for the as-delivered Forged bar specimen that showed great uniformity.

All building directions in the as-printed condition were tested. Two planes of the as-printed specimens were tested, as seen in Figure 3.4. X-direction is used for all other hardness tests. Hardness tests on specimens of building direction H and D as well as the Forged bar specimen were made after the solution annealing heat treatment to check if hardness were reduced. All

building directions and the Forged bar specimen in the heat treated condition (solution annealed and age hardened) were tested.
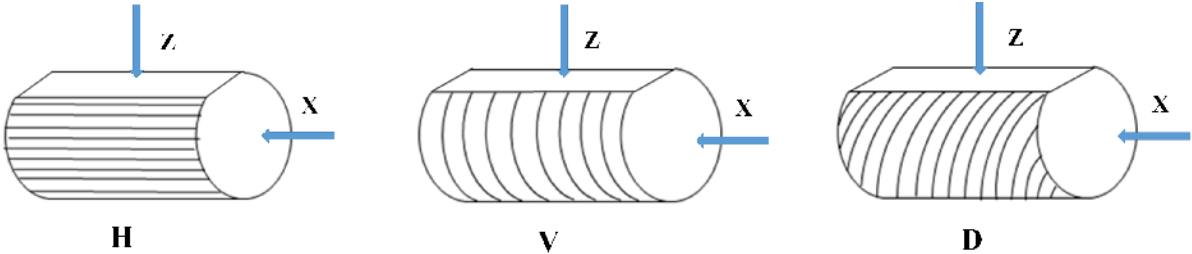
Figure 3.4: Test planes for hardness tests.

Samples were grinded and polished before indentations to make the test surfaces as smooth as possible. This to ensure equal test conditions for every indentation in every specimen and to ensure that indentations were properly made.

3.6 Mechanical properties

Chemical composition analysis of the additive manufactured material with the use of Positive Material Identification (PMI) are presented in Table 3.2 below. Note that only the main alloying elements are detected ($> 1wt\%$).

Table 3.2: Chemical composition in wt% measured with PMI.

Element	Content
Ni	52.35
Cr	19.15
Fe	18.35
Nb	5.58
Mo	3.37
Ti	1.20

Tables 3.3 – 3.7 below presents technical data and standards for additive manufactured materials. Table 3.8 below presents manufacturer test values for the forged bar.

Table 3.3: ASTM F3055 as-printed (class A). Minimum tensile properties.

Specimen	Rp0.2 [MPa]	Rm [MPa]	A [%]	Z [%]	E [GPa]
Horizontal direction	635	980	27	-	
Vertical direction	600	920	27	-	

Table 3.4: ASTM F3055 heat treated (class F). Minimum tensile properties.

Specimen	Rp0.2 [MPa]	Rm [MPa]	A [%]	Z [%]	E [GPa]
Horizontal direction	940	1240	12	-	
Vertical direction	920	1240	12	-	

Table 3.5: Eosint technical data for as-printed condition. All typical values.

Specimen	Rp0.2 [MPa]	Rm [MPa]	A [%]	Z [%]	E [GPa]
Horizontal direction	780 ± 50	1060 ± 50	27 ± 5	-	160 ± 20
Vertical direction	634 ± 50	980 ± 50	31 ± 5	-	

Table 3.6: Eosint technical data. Heat treatment per AMS 5664, not the same as conducted in this experiment. All typical values.

Specimen	Rp0.2 [MPa]	Rm [MPa]	A [%]	Z [%]	E [GPa]
Heat treated	1240 ± 100	1380 ± 100	18 ± 5	-	170 ± 20

Table 3.7: SLM technical data for as-printed condition.

Specimen	Rp0.2 [MPa]	Rm [MPa]	A [%]	Z [%]	E [GPa]
As printed	689 ± 67	995 ± 43	29 ± 4	47 ± 4	173 ± 17

Table 3.8: Forged bar quality release note.

Specimen	Rp0.2 [MPa]	Rm [MPa]	A [%]	Z [%]	E [GPa]
Forged bar	899	1242	32	52	

Rp0.2 is Yield strength (0.2% offset), MPa

Rm is Tensile strength (UTS), MPa

A is Elongation at break, %

Z is contraction at fracture, %

4 Results

4.1 Tensile Tests

Results from the tensile tests are presented below. Table 4.1 shows the test values of the as-printed condition. Table 4.2 shows the test values of the heat treated condition. Table 4.3 shows the test values of the forged bar in the as-delivered condition.

Table 4.1: Tensile test values for additive manufactured specimens in the as-printed condition..

Specimen	Rp0.2 [MPa]	Rm [MPa]	A [%]	Z [%]	E [GPa]
H P	784	1090	29.5	48	190.217
D P	747	1080	33.2	39	211.165
V P	648	1014	34.7	51	238.216
SH P	669	989	31.0	39	185.594

Table 4.2: Tensile test values for additive manufactured specimens in the heat treated condition.

Specimen	Rp0.2 [MPa]	Rm [MPa]	A [%]	Z [%]	E [GPa]
H H	1177	1405	20.0	29	203.897
D H	1178	1410	21.2	33	223.703
V H	1130	1327	19.6	39	187.618
SH H	1102	1287	22.0	33	189.851

Table 4.3: Tensile test values for forged bar specimens in the as-delivered condition.

Specimen	Rp0.2 [MPa]	Rm [MPa]	A [%]	Z [%]	E [GPa]
FB 1	907	1249	34.0	54	209.423
FB 2	888	1246	32.8	54	196.517

Rp0.2 is Yield strength (0.2% offset), MPa

Rm is Tensile strength (UTS), MPa

A is Elongation at break, %

Z is contraction at fracture, %

Tensile test values are presented in diagrams below. Figure 4.1 shows yield and tensile test values for all test specimens. Figure 4.2 shows the values of elongation at break and contraction at fracture for all test specimens. Figure 4.3 shows the values of modulus of elasticity for all test specimens.
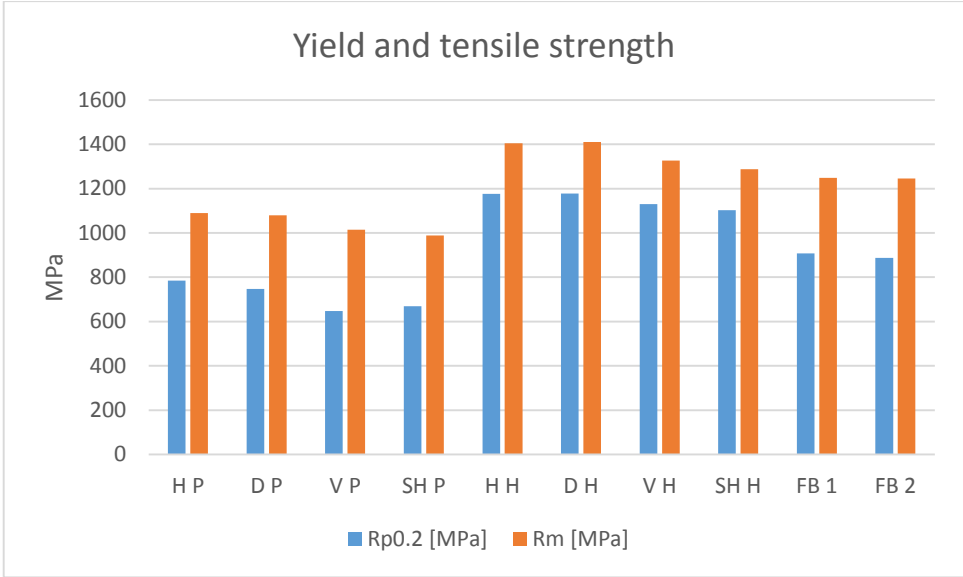
Figure 4.1: Yield and tensile strength values for all test specimens.
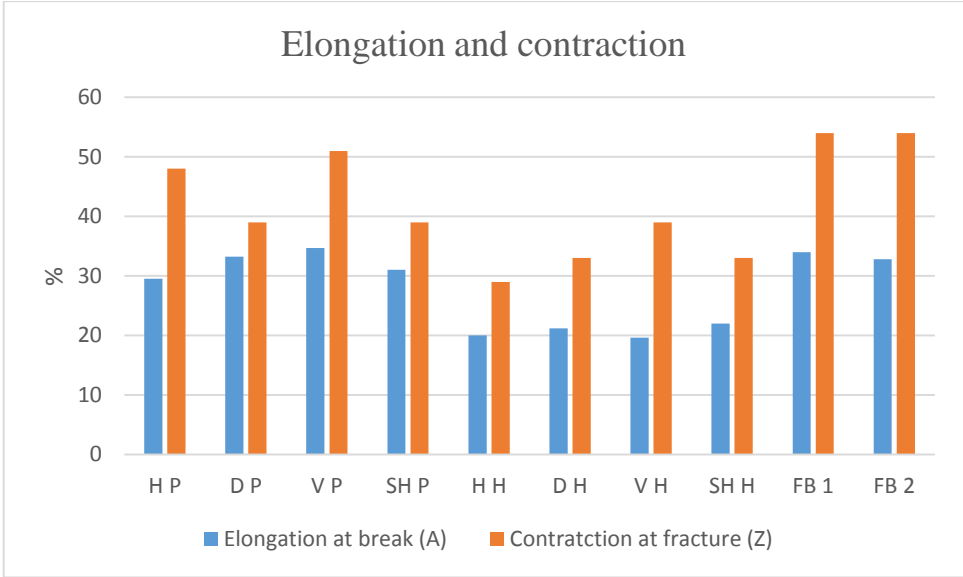
Figure 4.2: Values of elongation at break and contraction of fraction for all test specimens.
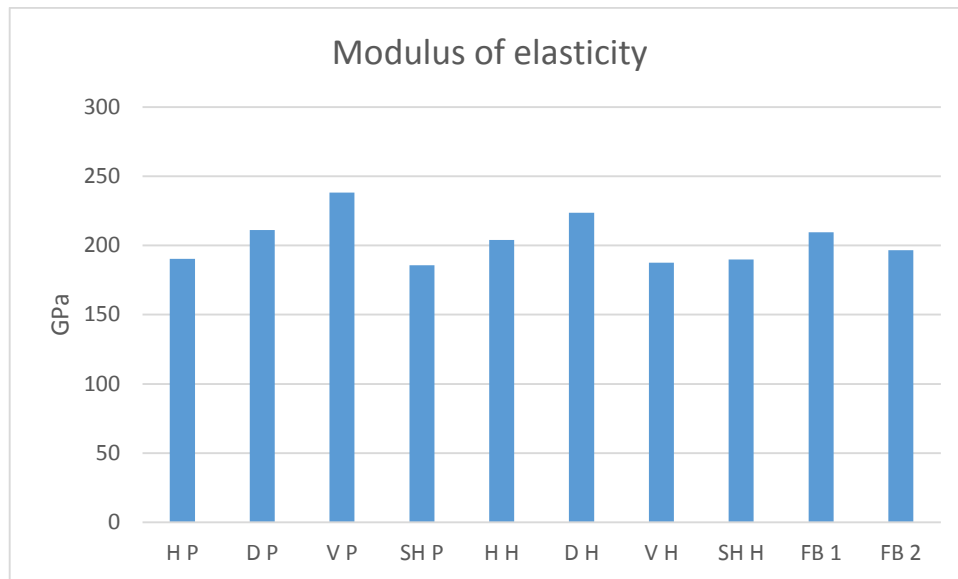
Figure 4.3: Values of modulus of elasticity for all test specimens.

4.1.1   As-printed Condition

4.1.1.1   *Eosint Printed Specimens:*

Specimen H P has the higher tensile (R_m) and yield ($R_{p0.2}$) strength, the lower percentage of elongation at break (A) and modulus of elasticity (E), and the middle percentage of contraction at fracture (Z).

Specimen D P:has the middle tensile and yield strength, percentage of elongation at break and modulus of elasticity, and the lower percentage of contraction at fracture.

Specimen V P has the lower tensile and yield strength, the higher percentage of elongation at break, percentage of contraction at fracture and modulus of elasticity.

Specimen H P is the stronger specimen in terms of yield and tensile strength as seen in Figure 4.1. The tensile and yield strength values of specimen V P is considerably lower than for specimen D P and H P. Specimen D P and H P seem to be of similarity, while specimen V P stands a little out. The percentage of elongation at break, percentage of contraction at fracture and modulus of elasticity of specimen V P as seen in Figure 4.2 and Figure 4.3 indicates that this specimen is more ductile than specimen H P and D P.

All test values are within the range of the technical data provided by the manufacturer, except for modulus of elasticity for specimen H which are larger than the range suggested. All test

values meet the requirements of ASTM F3055, "Standard Specification for Additive Manufacturing Nickel Alloy (UNS N07718) Power Bed Fusion", for class A.

4.1.1.2   *SLM Printed Specimen Compared to the Eosint H Specimen:*

The SLM printed specimen SH P has a yield strength that is less than a 100 MPa of the Eosint printed specimen H P as seen in Figure 4.1. The tensile strength is almost equal to 100 MPa less than the Eosint printed specimen H P. The Eosint printed specimen H P is superior to the SLM printed specimen SH P in terms of yield and tensile strength. The values are far greater.

The SLM printed specimen SH P has the higher percentage of elongation at break as seen in Figure 4.2. However, percentage of elongation at break is quite similar for the two specimens. The SLM printed specimen SH P has the lower percentage of contraction at fracture and modulus of elasticity. However, modulus of elasticity is, as seen in Figure 4.3, almost equal for the two.

The percentage of elongation at break and percentage of contraction at fracture values are inconsistent. The SLM printed specimen SH P has the higher percentage of elongation at break and the lower percentage of contraction at fracture giving no clear indication on which one is more ductile.

All test values of the SLM printed specimen SH P, with the exception of the percentage of contraction at fracture, are within the range of the technical data provided by the manufacturer. The range presented in the technical data suggest a minimum of 43 % contraction at fracture. The SLM printed specimen SH P was contracted 39 % at fracture, 4 % less than suggested. All test values of the SLM printed specimen SH P meet the requirements of ASTM F3055, "Standard Specification for Additive Manufacturing Nickel Alloy (UNS N07718) Power Bed Fusion", for class A. Technical data provided by Eosint and SLM show that Eosint specimens are superior to SLM. This is confirmed by the test results.

4.1.2   Heat treated Condition

4.1.2.1   *Eosint Printed Specimens:*

Specimen H H has the middle tensile and yield strength, percentage of elongation at break and modulus of elasticity, and the lower percentage of contraction at fracture.

Specimen D H has the higher tensile and yield strength, percentage of elongation at break and modulus of elasticity, and the middle percentage of contraction at fracture.

Specimen V H has the lower tensile and yield strength, percentage of elongation at break and modulus of elasticity, and the higher percentage of contraction at fracture.

The tensile and yield strength values of specimen V H is, as seen in Figure 4.1, noticeably lower than for specimen D H and H H. Yield and tensile strength values of specimen H H are almost equal to the values of specimen D H. However, values of specimen D H are slightly higher. Percentage of elongation at break is, as seen in Figure 4.2, almost equal for all three specimens. Specimen H H and D H still seem to be the most similar of the three.

The heat treatment has clearly made changes in mechanical properties. All specimens have increased their yield strength by at least 50 % and tensile strength by about 30 %. This at the cost of ductility. Contraction and elongation percentages of the specimens has decreased considerably. Modulus of elasticity, as seen in Figure 4.3, have increased slightly for all specimens, except for specimen V which has a remarkable decrease of 20 %. Values show that specimen V H has the larger percentage of increase of yield and tensile strength, while specimen H H has the lower percentage of increase of yield and tensile strength. Values show that specimen D H has become the stronger specimen. However, it is only by a fraction. Specimen D H and H H seem to be equal. Specimen V H seem to be the weaker specimen. Even though it has the larger percentage of increase and the greater actual increase value of yield strength, it still has considerable lower yield and tensile strength compared to specimen D H and H H. In addition, its favorable ductility is lost.

All test values, with the exception of yield strength of specimen V H and modulus of elasticity of specimen H H which has a value greater than suggested, are within the range of the technical data provided by the manufacturer. Note that the provided technical data applies to a heat treatment with other parameters than performed in this study. All test values meet the requirements of ASTM F3055, "Standard Specification for Additive Manufacturing Nickel Alloy (UNS N07718) Power Bed Fusion", for class F.

4.1.2.2   SLM Printed Specimen Compared to the Eosint Printed H Specimen:

The SLM printed SH H specimen has the lower yield strength of the two. The tensile strength of the SLM printed specimen SH H is about 120 MPa less than the Eosint printed H H. The

SLM printed specimen SH H has the higher percentage of elongation at break and percentage of contraction at fracture. However, these values are not very differing for the two specimens. The SLM printed specimen SH H has the lower modulus of elasticity.

The SLM printed specimen SH H has the larger increase in yield strength. The tensile strength has increased by 30 % for both specimen. However, the Eosint printed specimen H H has the larger actual increase value of tensile strength. The Eosint printed specimen H H is the stronger specimen when yield and tensile strength are considered. Values show that the ductility has been reduced for both specimen. However, modulus of elasticity have increased slightly for both specimens. The SLM printed specimen SH H has the larger values of percentage of contraction at fracture and elongation at break, indicating that this specimen is more ductile. However, only a few percentage points divides the two specimens. The Eosint printed specimen H H has been more affected by the heat treatment in terms of loss of ductility. Both the reduction of percentage and percentage points of contraction at fracture and elongation at break favors the SLM printed specimen SH H as this specimen has the lower reduction. All test values meet the requirements of ASTM F3055, "Standard Specification for Additive Manufacturing Nickel Alloy (UNS N07718) Power Bed Fusion", for class F.

4.1.3 Reference Specimens

Values for both specimen are quite similar. Yield strength has a difference of about 30 MPa. Tensile strength is almost equal. Percentage of elongation at break has a difference of 1.2 percentage points. Percentage of contraction at fracture is equal. No values stands out. The reference specimens are in accordance with the quality control release note provided by the manufacturer. It shows that the material is uniform. It also confirms that the experimental test method carried out is acceptable.

4.1.4 Effect of Heat Treatment on Tensile Properties

The effect of heat treatment of additive manufactured specimens are presented below. Table 4.4 shows the quantitative effect of heat treatment of additive manufactured specimens. Table 4.5 shows the effect of heat treatment of additive manufactured specimens in percentage.

Table 4.4: Quantitative effect of heat treatment of additive manufactured specimens. Note that values of A and Z are given in percentage points.

Build direction	Rp0.2 [MPa]	Rm [MPa]	A [%]	Z [%]	E [GPa]
H	393	315	-9.5	-19	13.68
D	431	330	-12.0	-6	12.538
V	482	313	-15.1	-12	-50.598
SH	433	298	-9.0	-6	4.257

Table 4.5: Effect of heat treatment of additive manufactured specimens in percentage.

Build direction	Rp0.2	Rm	A	Z	E
H	50.1	28.9	-32.2	-39.6	7.2
D	57.7	30.6	-36.1	-15.4	5.9
V	74.4	30.9	-43.5	-23.5	-21.2
SH	64.7	30.1	-29.0	-15.4	2.3

The effect of heat treatment of additive manufactured specimens are presented in the diagram below. Figure 4.4 shows the effect of heat treatment of additive manufactured specimens.
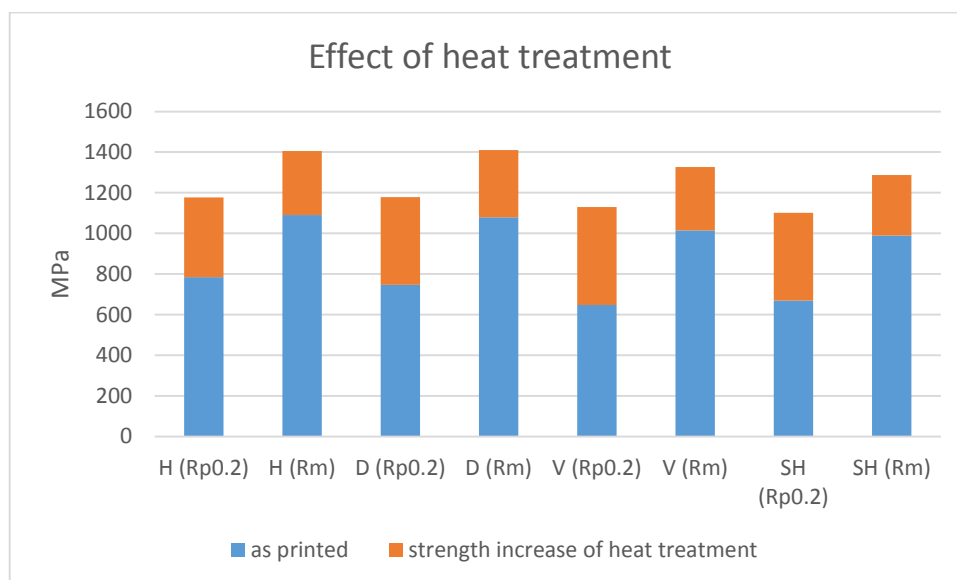

Figure 4.4: The effect of heat treatment.

Every specimen has a large increase in tensile and yield strength. Yield strength has increased by about 50 – 75 % for all specimen. Tensile strength has increased by about 30 % for all

specimen. All specimens has a decreased percentage of elongation at break, ranging from 29 – 43.5 % reduction. All specimens has a decreased percentage of contraction at fracture, ranging from about 15 – 40 % reduction. Modulus of elasticity has increased slightly in specimen H, D and SH, while specimen V has a decrease of a little more than 20 %.

Heat treatment of the printed specimens has clearly made them stronger. Yield and tensile strength has been increased to values significantly larger than specimen FB and mechanical properties suggested by conventional Inconel 718 producers. However, this at the cost of ductility. Contraction at fracture and elongation at break suggest that the heat treated printed material is less ductile than specimen FB and mechanical properties suggested by conventional Inconel 718 producers. This leads to the conclusion that the heat treatment of the printed specimens only are partially successful. Mechanical properties that a conventionally produced Inconel 718 alloy holds, was not fully achieved.

The statistical data basis of all tests are not sufficient. One test sample is not sufficient even though the values are within the range of acceptance. More samples should be tested in order to provide an acceptable statistical basis.

4.2   Hardness

Test planes for hardness tests were presented in chapter 3.5 Figure 3.4: Test planes for hardness tests. Hardness test average values and standard deviation for all tests are presented in tables and diagrams in this chapter. All test values are presented in Appendix B. Table 4.6 below shows the hardness test values in the x-plane for all build directions in the as-printed condition and forged bar in the as-delivered condition.

Table 4.6: Hardness test values in the X-plane for all build directions in the as-printed condition and the forged bar in the as-delivered condition.

	Forged bar	V P	H P	D P
Average	380.6	308.6	319.6	305.1
Standard deviation	1.1	11.9	6.9	9.9

Specimen H has the higher average hardness, specimen V has the middle average hardness and specimen D has the lower average hardness. Specimen V has the higher standard

deviation, specimen D has the middle standard deviation and specimen H has the lower standard deviation. The highest measured value is 327 HV, measured in specimen D P. The lowest measured value is 288 HV, measured in specimen V P.

The forged bar as-delivered has low standard deviation and no distinguishes itself. It is much harder than the as printed specimens.

Table 4.7 below shows the hardness test values in the z-plane for all build directions in the as-printed condition.

Table 4.7: Hardness test values in the Z-plane for all build directions in the as-printed condition.

	V P	H P	D P
Average	301.0	296.4	295.1
Standard deviation	11.0	3.6	14.7

Specimen V has the higher average hardness, specimen H has the middle average hardness and specimen D has the lower average hardness. Specimen D has the higher standard deviation, specimen V has the middle standard deviation and specimen H has the lower standard deviation. The highest value measured is 327 HV, measured in specimen D. The lowest value measured is 283 HV, measured in specimen D.

Hardness values of the additive manufactured specimens in the as-printed condition of both x-plane and z-plane are presented in Figure 4.5 below. Figure 4.6 shows the yield and tensile strength for all build directions in the as-printed condition. The figure is presented to compare the hardness and tensile properties to each other and detect a possible connection.
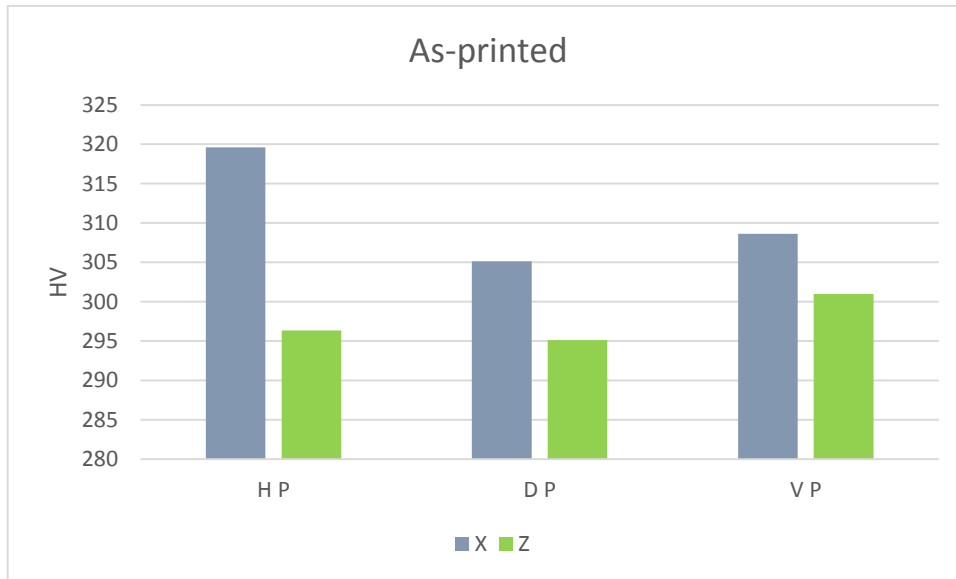
Figure 4.5: Comparison of the three build directions in the as-printed condition for the two test planes.
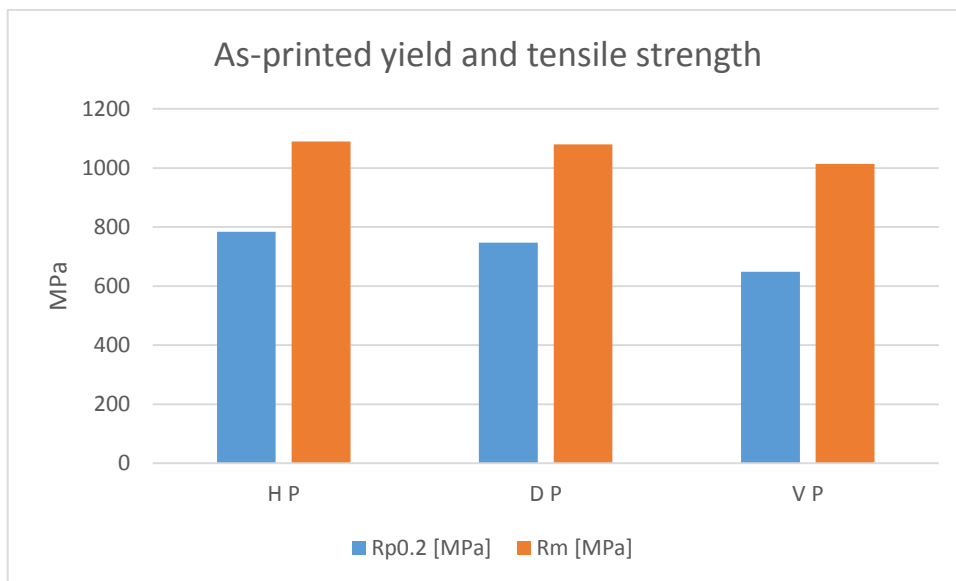
Figure 4.6: Yield and tensile strength of the as-printed condition for the three build directions.

Figure 4.5 illustrates that all specimens are harder in the x-plan than the z-plane. It also states specimen H P is the hardest of the three and V P the softest. Figure 4.6 shows that specimen H P is the strongest of the three in terms of yield and tensile strength and specimen V P is the weakest. Values indicates that there is a connection between hardness and yield and tensile properties.

Table 4.8 below shows the hardness values of specimens in the solution annealed condition.

Table 4.8: Hardness values of build directions H and D and the forged bar in the solution annealed condition.

	Forged bar	H	D
Average	168.4	258.3	262.5
Standard deviation	3.2	2.6	3.5

Specimen D has higher average hardness than specimen H. Printed specimens has higher average hardness than the Forged bar specimen. Specimen D has the higher standard deviation. The highest value measured is 269 HV, measured in specimen D. The lowest value measured in the printed specimens is 255 HV, measured in specimen H. Standard deviation of the Forged bar specimen is similar to the printed specimens.

The annealing process has softened the material. Average hardness of the printed specimens has decreased by about 40 – 60 HV. Compared to the specimen FB, which has decreased by about 210 HV, is the hardness reduction of the printed specimens very low.

The standard deviation indicates that the solution annealing has made the printed specimens more uniform/homogenous.

Table 4.9 below shows the hardness values of specimens in the age hardened condition.

Table 4.9: Hardness values of all build directions and the forged bar in the age hardened condition.

	Forged bar	V H	H H	D H
Average	386.6	414.8	421.5	429.8
Standard deviation	2.9	5.1	5.4	7.0

Specimen D has the higher average hardness, specimen H has the middle average hardness and specimen V has the lower average hardness. Printed specimens has higher average hardness than the Forged bar specimen. Specimen D has the higher standard deviation, specimen H has the middle standard deviation and specimen V has the lower standard deviation. The highest value measured is 440 HV, measured in specimen D. The lowest value

measured in the printed specimens is 406 HV, measured in specimen V. Standard deviation of the Forged bar specimen is lower than the printed specimens.

Hardness values for all specimens in the x-plane are presented in Figure 4.7 below.
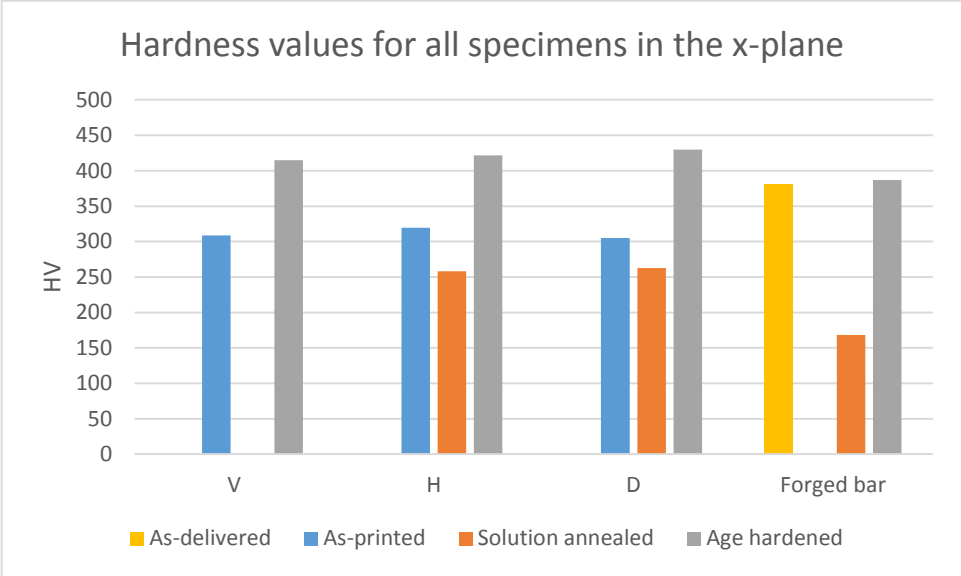
Figure 4.7: x-plane hardness values for all specimens.

The age hardening process has clearly hardened the material. Printed specimens has increased average hardness by more than 100 HV from the as printed condition and about 160 HV from the solution annealed condition.

The standard deviation indicates that the printed material has become more uniform/homogeneous in the age hardened condition than in the as printed condition. However, less homogenous than in the solution annealed condition.

The Forged bar specimen has returned to its starting point. It has nearly the exact same average hardness value as it had before the repeated heat treatment, indicating that the heat treatment process has been successful. Standard deviation has increased slightly from before the second heat treatment.

The age hardening process has made the printed specimen harder than the forged bar reference specimen. Standard deviation for the printed specimens are larger than for the forged bar specimen, indicating that the printed material need different heat treatment

parameters in order to obtain the same mechanical properties as specimen FB and mechanical properties suggested by conventional Inconel 718 producers. This, as well as the tensile tests, suggests that the heat treatment of the printed specimens only were partially successful.

4.3   Microstructure

4.3.1   Optical Light Microscope

Optical light microscopy examination of all test specimens are presented in this chapter. As stated in chapter 3.3, all specimens are examined in the x-plane as seen in Figure 3.2. Figure 4.8 below shows the microstructure of the forged bar in the as-delivered condition.
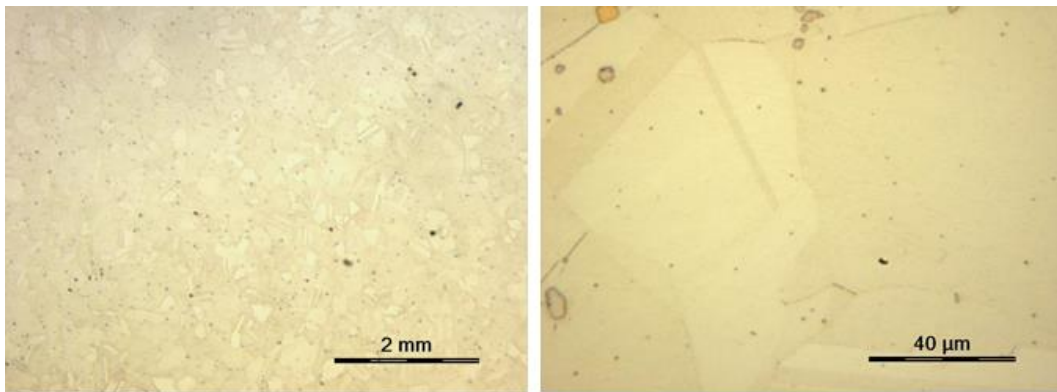
Figure 4.8: Forged bar specimen in the as-delivered condition.

The microstructure of the forged bar in the as-delivered condition has grain boundaries of straight character. The microstructure show carbide precipitation. The carbides seem to be evenly and arbitrarily distributed. No signs of δ-phase precipitation. Yellow/orange rectangular looking precipitates, as seen in Figure 4.8 right, are found randomly distributed. Chapter 2.3.2.11 describes square shaped precipitates with an appearance ranging from orange to yellow as MN nitride precipitates. These nitrides are easily spotted as-polished, indicating that N is present in the material. Heat treatment of the material did not dissolve these precipitates, which is in accordance with theory as these nitrides are insoluble at temperatures below the melting point.

Below are the microstructure of all build directions in the as-printed condition presented. Figure 4.9 shows the microstructure of specimen H P, Figure 4.10 shows the microstructure of specimen V P and Figure 4.11 shows the microstructure of specimen D P.

Figure 4.9: Light microscope examination of specimen H P (as-printed).

Figure 4.10: Light microscope examination of specimen V P (as-printed).

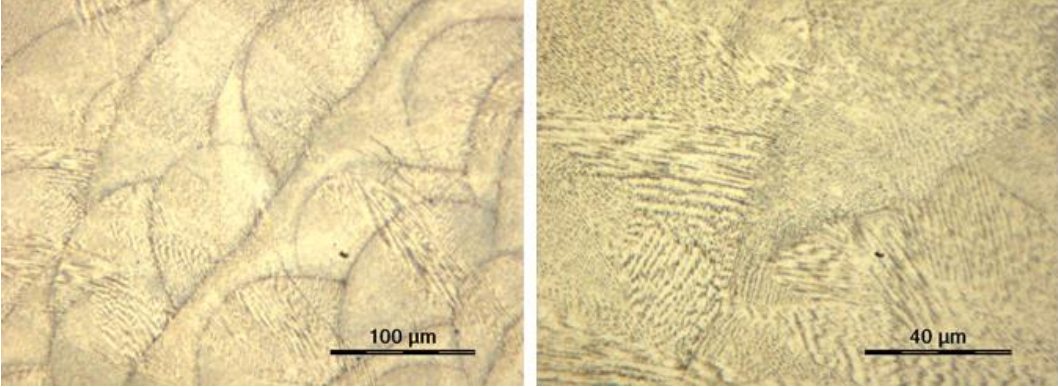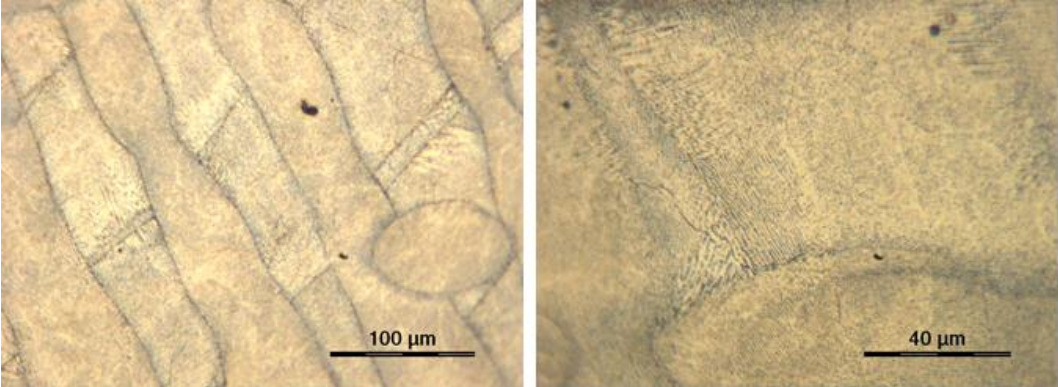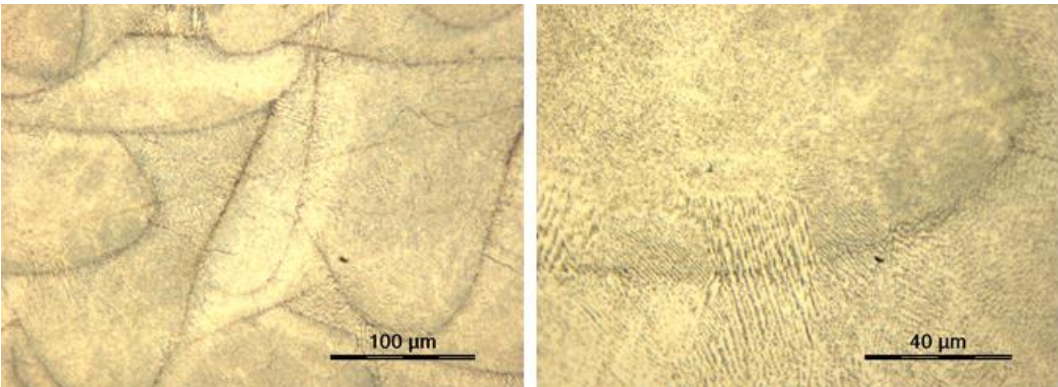*Figure 4.11: Light microscope examination of specimen D P (as-printed).*

Each layer is easily observed in all specimens. Most layers in specimen H P and D P, as seen in Figure 4.9 and Figure 4.11, have one parabolic side and one more flat side. Some layers are stretched out as long columnar layers. In specimen V P, Figure 4.10, are all layers stretched out as long columnar layers. The specimens show that the layers are not printed in the same direction. Specimen V P clearly show that the layers are crossing each other. Hence, when a new layer is put on top of another, the laser movement direction is changed. Analysis of the microstructure indicates that three different directions are used. In other words, if the first layer is melted by horizontal laser movement is the second layer melted by a laser movement 120 degrees to the horizontal movement. Specimens H and D supports this as shape of the layers varies, proving different printing angels in the x-y plane.

The specimens show elongated dark lines which are believed to be microcracks. Microcracks seem to develop in connection with the boundary of a layer. However, some microcracks are observed inside single layers.

Dark dots and short straight lines are observed all over and seem evenly distributed. The lines are observed to point in certain directions in various areas of the microstructure. An area where lines point in the same direction may be a grain. Dots and lines are believed to be Laves precipitates. Light areas are likely to be dendritic γ. No visual evidence of carbides or δ precipitation. However, dark spots are very occasionally observed.

The upper right corner in Figure 4.10 right of specimen V P shows a spot of size about 5 - 10 µm long which appear yellow/orange. This may be an MN precipitate as mentioned above, a slight indication of fractions of N impurities. However, this is only observed once in the specimen.

Below are the microstructure of all build directions in the heat treated condition presented. Figure 4.12Figure 4.9 shows the microstructure of specimen H H, Figure 4.13 shows the microstructure of specimen V H and Figure 4.14 shows the microstructure of specimen D H.
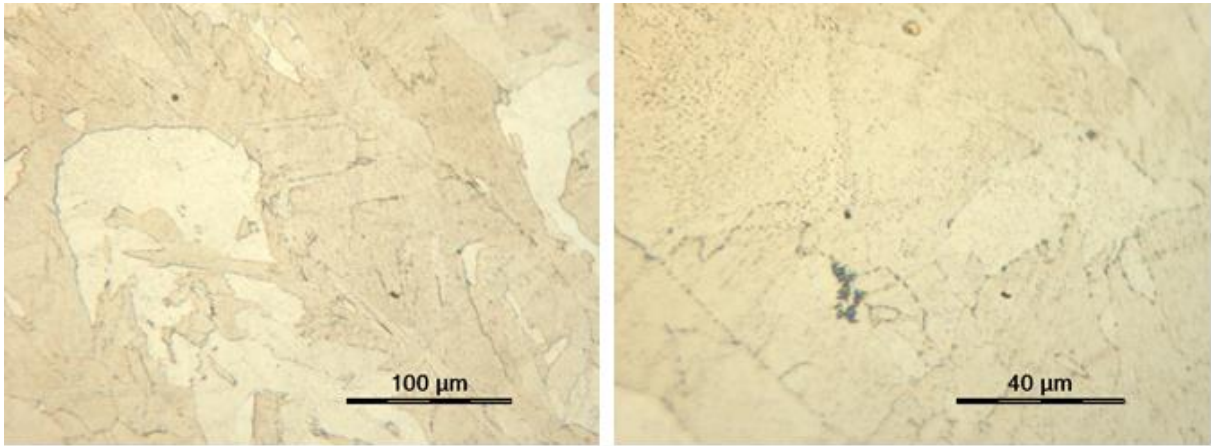
Figure 4.12: Light microscope examination of specimen H H (solution annealed and precipitation hardened).
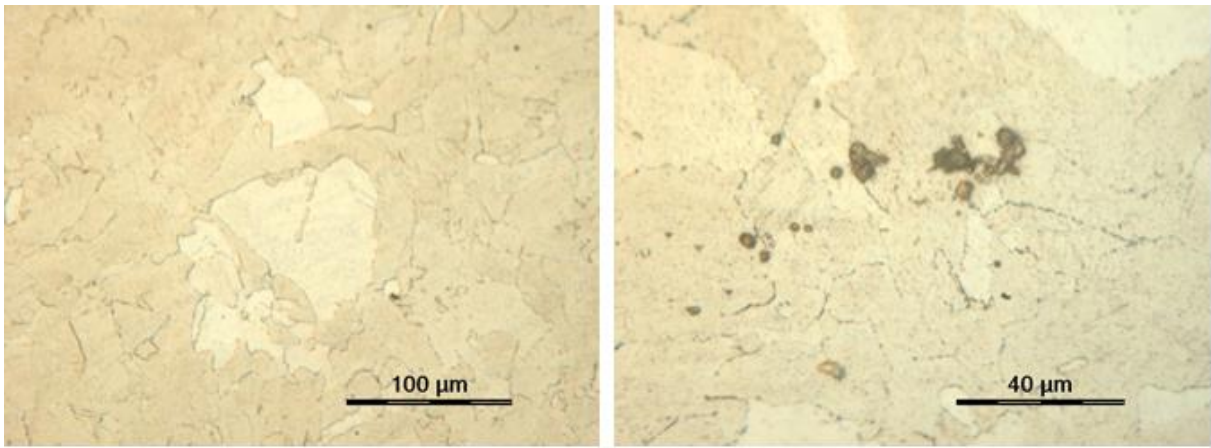

Figure 4.13: Light microscope examination of specimen V H (solution annealed and precipitation hardened).
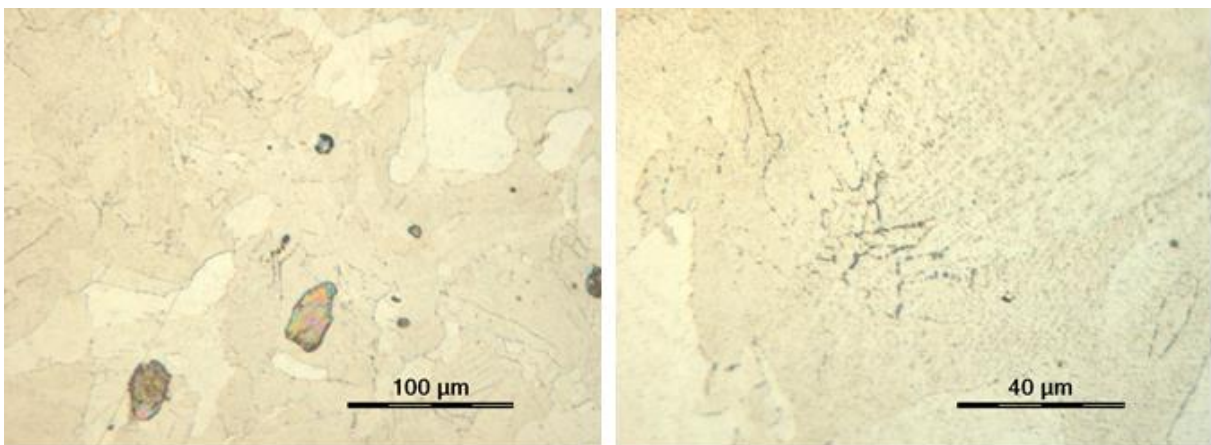
Figure 4.14: Light microscope examination of specimen D H (solution annealed and precipitation hardened).

57

Grain boundaries in all heat treated additive manufactured specimens seem to be of some straight character, appearing more similar to the microstructure of the forged bar. The layer structure from the printing process is erased. The microstructure show carbide precipitation both as particles and on grain boundaries. The carbides seem to be arbitrarily distributed. No visual evidence of δ precipitation or Laves phase. Yellow/orange appearing spots are very occasionally observed. The upper middle of Figure 4.12 to the right of specimen H H shows a circular spot that appear yellow/orange. This were also found in specimen V P (as-printed). Since MN precipitates are insoluble at temperatures below the melting point, it is likely that the yellow/orange appearing precipitate found in both specimens are MN precipitate.

4.3.2 Scanning Electron Microscopy

In this chapter are SEM images of various observations presented. As stated in chapter 3.3, all specimens are examined in the x-plane as seen in Figure 3.2. There are no difference observed between the additive manufactured specimens and there is no connection between build direction and images presented. Images presented are those that seem to provide most information and are of highest quality.

Figure 4.15 below shows the microstructure of specimen V P, V H and FB. Images are made by the use of the backscatter detector. The images are presented to show the dark spots, pores, and the bright spots, carbides, in the material.
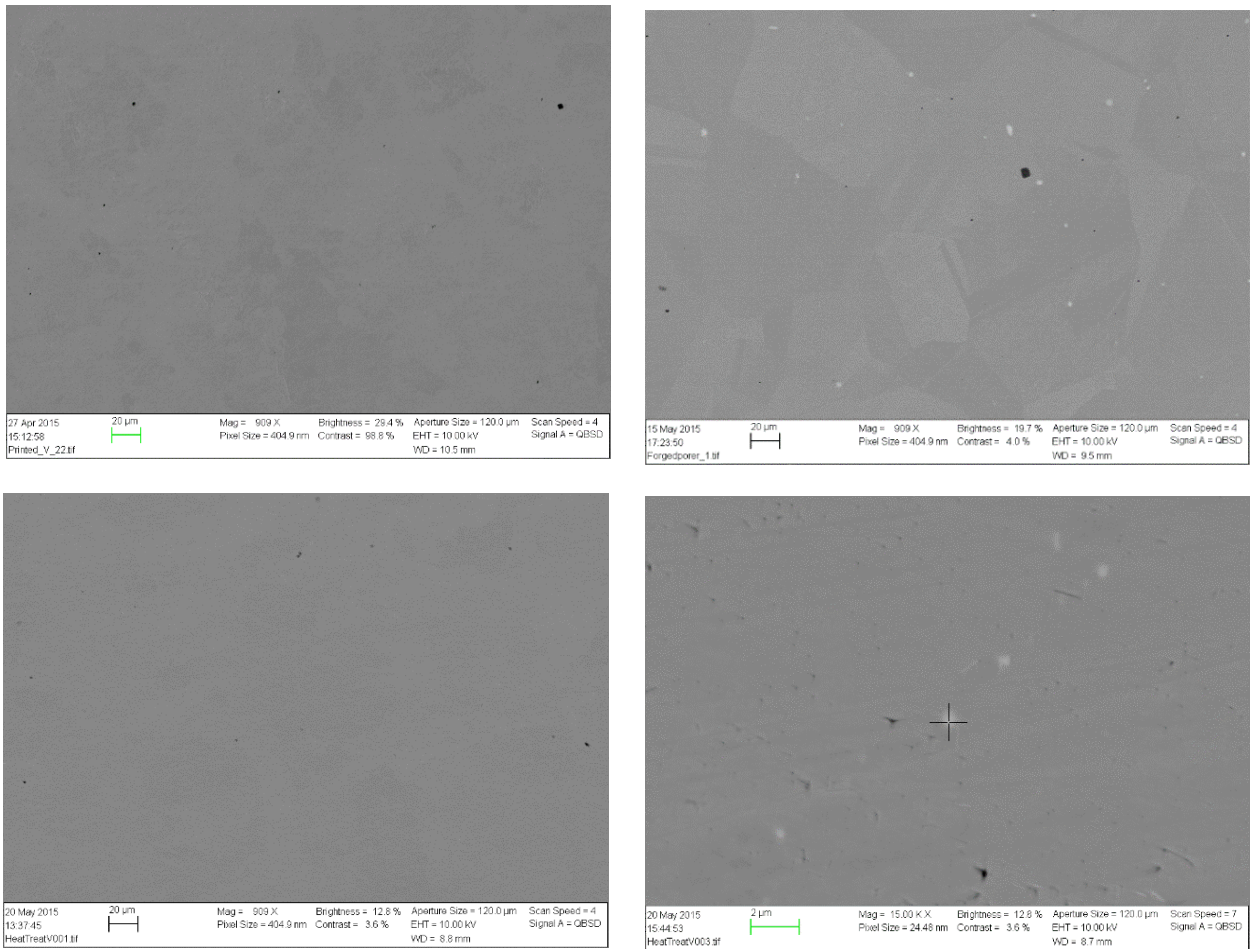
7

Figure 4.15: Top left: Specimen V P. Top right: Specimen FB. Bottom left and right: Specimen V H.

Bright spots are observed in the forged bar specimen and in specimen V H. Chemical composition of bright spots determined by analysis of characteristic x-rays are presented in Table 4.10 and Table 4.11.Bright spots in the heat treated additive manufactured specimen are much smaller than in the forged bar specimen. Note that the image at the bottom right has a higher primary magnification than the three others. A few dark spots are observed in every specimen. Chemical composition of a dark spot determined by analysis of characteristic x-rays are presented in Table 4.12.

59

Table 4.10: Chemical composition of a bright spot in the forged bar specimen determined by characteristic x-ray.

Element	wt%	at%
Al	0.04	0.14
Nb	79.14	72.7
Mo	9.71	8.63
Ti	6.45	11.49
Cr	1.07	1.75
Fe	0.88	1.35
Ni	2.7	3.93

Table 4.11: Chemical composition of a bright spot in the heat treated V specimen determined by characteristic x-ray

Element	wt%	at%
Nb	68.94	59.29
Mo	9.76	8.13
Ti	6.35	10.6
Cr	8.08	12.41
Fe	3.17	4.54
Ni	3.69	5.02

Table 4.12: Chemical composition of dark spot in the heat treated V specimen determined by characteristic x-ray.

Element	wt%	at%
Nb	5.31	3.37
Mo	3.9	2.39
Ti	0.93	1.14
Cr	16.64	18.85
Fe	16.05	16.92
Ni	57.17	57.34

Bright spots suggest compositions of heavy elements because bright spots are a result of more signal from that specific area than the surroundings. Chemical composition of bright spots as seen in Table 4.10 and Table 4.11 determined by analysis of characteristic x-rays show large amounts of Nb and, relative to alloy additions, Ti. These elements are typical for MC carbides. Chemical composition of dark spots as seen in Table 4.12 determined by analysis of characteristic x-rays is similar to the chemical composition of the alloy. This suggests that dark spots are pores. Few dark spots are observed in all specimens, hence all specimens have high density.

Figure 4.16 below shows defects in specimen V P. Images are made by the use of the backscatter detector.
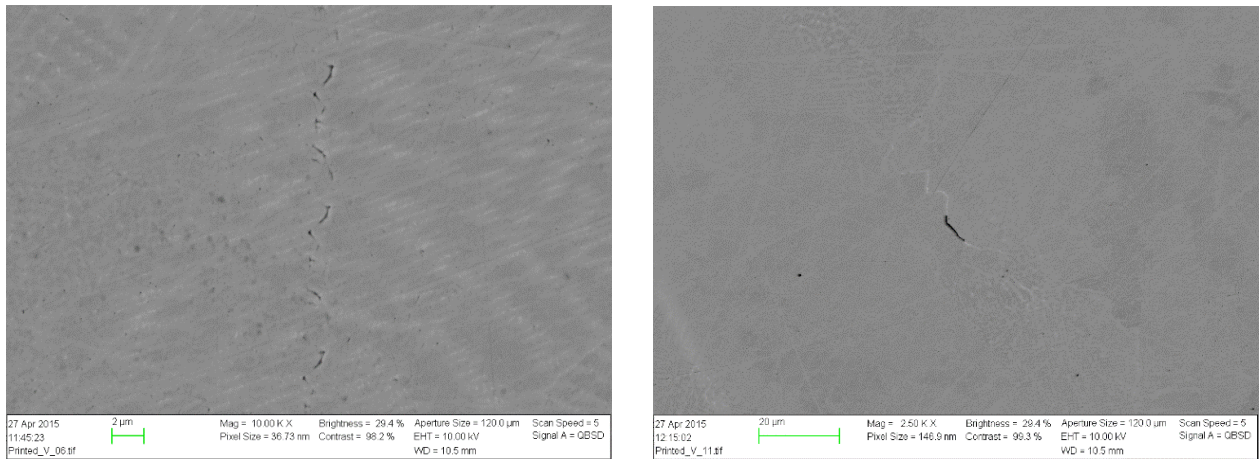
Figure 4.16: Both images shows defects in specimen V P.

The image to the left are showing signs that lack of fusion during the printing process may have occurred. However, this is very occasionally observed. The image to the right show a dark stretched area on a bright curvy line. Table 4.13 shows the chemical composition of the dark stretched area determined by analysis of characteristic x-rays.

Table 4.13: Chemical composition of the dark stretched area in specimen V P determined by characteristic x-ray.

Element	wt%	at%
Nb	8.07	5.09
Ti	1.35	1.65
Cr	16.12	18.17
Fe	14.75	15.49
Ni	59.70	59.59

Element	wt%	at%
Nb	15.22	9.90
Cr	15.69	18.24
Fe	14.55	15.74
Ni	54.53	56.12

The chemical composition of the dark stretched area as seen in Table 4.13 is similar to the chemical composition of the alloy. This suggest that the dark stretched area is a pore or a crack. The chemical composition of the curvy line as seen in Table 4.14 show segregation of Nb to the line. Increased amounts of Nb may be MC (NbC) carbide precipitation, indicating that the bright curvy line is a grain boundary because MC carbides often form in the solidification grain boundary regions. Increased amounts of Nb may also be Laves phase. However, only in small amounts as the A_2B stoichiometry of the Laves phase suggests 1/3 Nb. However, both constituents raises the solidification temperature range of solidification and promotes cracking. Hence, the dark stretched area may be a solidification crack.

Figure 4.17 below shows dendritic structure in specimen H P. Images are made by the use of the backscatter detector and the EDX detector.
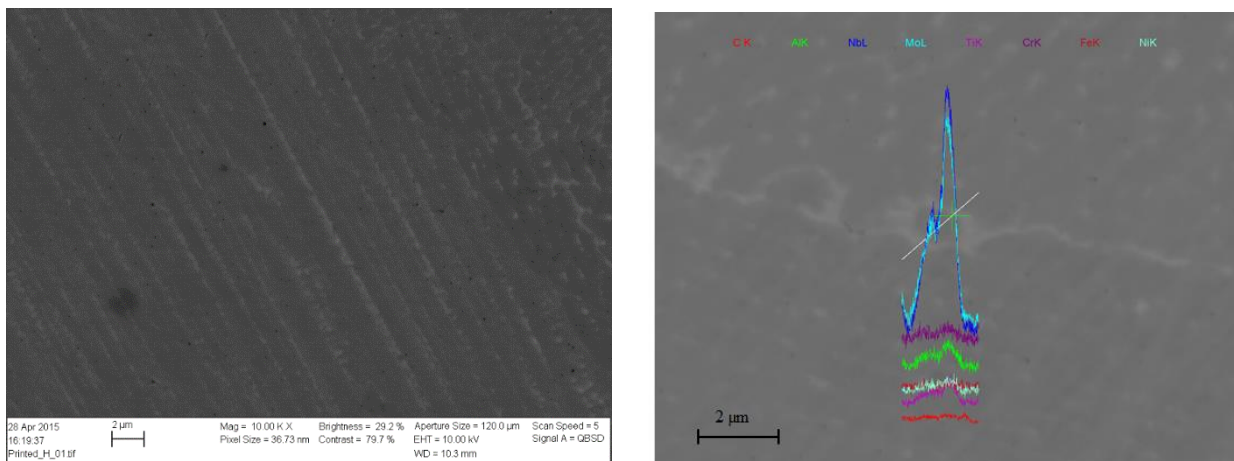
Figure 4.17: Both images show dendritic structure in specimen H P. The image to the right presents a line scan, made by the use of the EDX detector.

The image to the left of Figure 4.17 shows dendritic structure. The image to the right of Figure 4.17 shows an x-ray line scan of an interdendritic area. The line scan displays peaks of Mo and Nb in the bright areas. Bright areas are enriched by Mo and Nb. Mo and Nb are represented respectively by aqua blue and blue colors in the image.

Figure 4.18 shows specimen V P etched with a mix of hydrochloric acid and H_2O_2 for contrast.
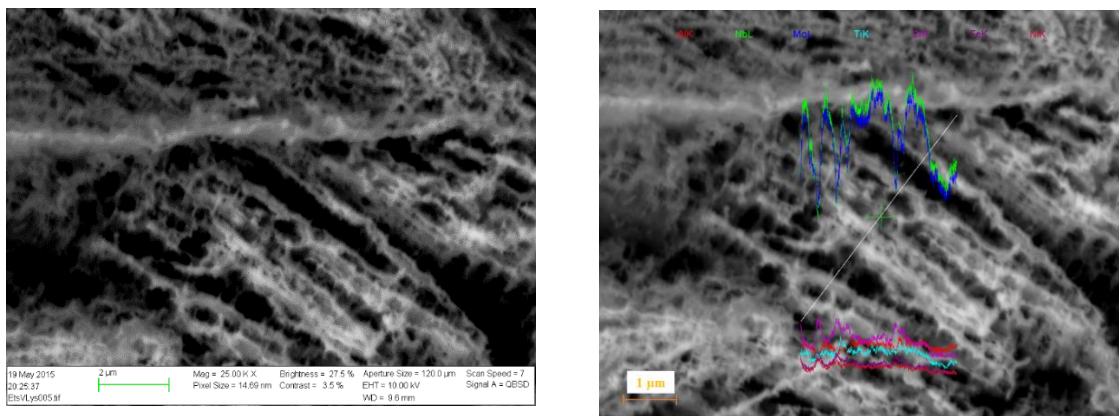
Figure 4.18: Image contrast provided by etching of specimen V P.

The x-ray line scan provided in Figure 4.18 to the right displays that the white areas are Mo and Nb rich, exactly as presented in Figure 4.17. Mo are represented by green and Nb are represented by blue in Figure 4.18. Chemical compositions of respectively bright, grey and dark areas in Figure 4.18 are presented in Table 4.15, Table 4.16 and Table 4.17 below.

Table 4.15: Chemical composition of bright white area in the as-printed etched V specimen determined by characteristic x-ray.

Element	wt%	at%
Nb	36.75	27.2
Mo	9.75	6.99
Ti	3.99	5.72
Cr	10.51	13.9
Fe	8.57	10.55
Ni	30.43	35.64

Table 4.16: Chemical composition of grey area in the as-printed etched V specimen determined by characteristic x-ray.

Element	wt%	at%
Nb	32.9	23.93
Mo	9.32	6.56
Ti	3.11	4.39
Cr	11.02	14.32
Fe	9.46	11.45
Ni	34.18	39.35

Table 4.17: Chemical composition of black area in the as-printed etched V specimen determined by characteristic x-ray.

Element	wt%	at%
Nb	20.31	13.74
Mo	5.92	3.88
Ti	2.76	3.63
Cr	14.6	17.64
Fe	13.05	14.69
Ni	43.36	46.42

The x-ray analysis suggests that several alloying elements have been attacked by the etchant. Amounts of Nb and Mo are remarkably large in the area where the etchant has made the largest impact.

Bright white areas contain large amounts of Nb and Mo. The amount of Nb and Mo are lower in the grey area and amounts are even lower in the black area. Wt% of Ni is lower in the white area than in the black.

The Laves phase has an A_2B stoichiometry $(Fe,Ni,Cr)_2(Nb,Mo,Si)$. The atomic percentage found by x-ray analysis of the white areas shows about 33at% of the elements Nb and Mo, as the B of the stoichiometry suggests for Laves phase. The rest consists of Fe, Ni and Cr, with the exception of some Ti, which makes the A_2 of the stoichiometry. This indicates that the bright white areas are Laves phase. Grey areas may be eutectic gamma following the L → γ + Laves eutectic reaction. Black areas may be gamma dendrite L→ γ solidification which appear prior to the eutectic reaction.

4.4   Crystallographic Orientation

In this chapter are crystallographic orientation and diffraction intensity presented. As stated in chapter 3.3, all specimens are examined in the x-plane as seen in Figure 3.2. Images to the left in all figures are OMs showing crystallographic orientation of every grain. Images to the right in all figures are diffraction intensity images, providing grain boundaries and grain structure.

The electropolishing did not polish equally over the sample surfaces. Images were therefore made from areas that were properly polished. Signal could only be detected in areas where the amorphous layer, a layer with no long-range regularity in its atomic structure, were removed.

In Figure 4.19 below is the inverse pole figure applicable to all OMs presented. It is a mix of red, blue and green. The grain color in OMs are decided by its crystallographic orientation.
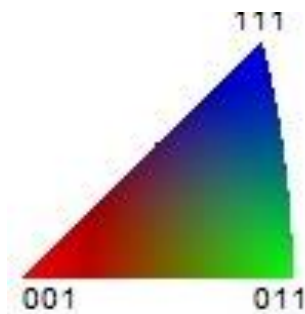
Figure 4.19: Inverse pole figure,

Figure 4.20 below shows the OM and diffraction intensity image of specimen FB.
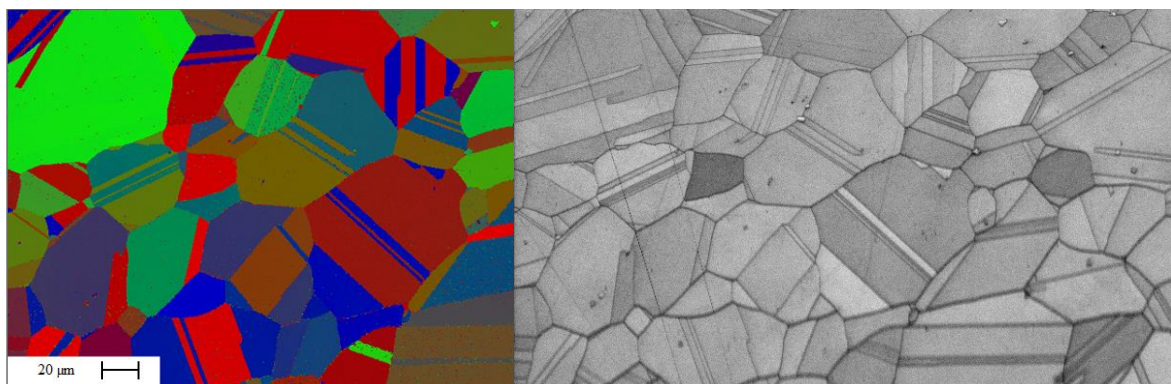
Figure 4.20: Forged bar specimen.

The forged bar specimen shows colors in the entire spectrum green, blue and red. Figure 4.20 shows that the colors are evenly distributed. No indication of specific crystallographic orientations of grains. Grain boundaries are well defined straight lines. All grains have one clear color. Twins are observed. Grain shape is edgy.

Below are images of the as-build additive manufactured specimens presented. Figure 4.21, Figure 4.22 and Figure 4.23 shows OMs and diffraction intensity images of specimen H P, V P and D P respectively.

Figure 4.21: Specimen H P.

Figure 4.22: Specimen V P.

Figure 4.23: Specimen D P.

67

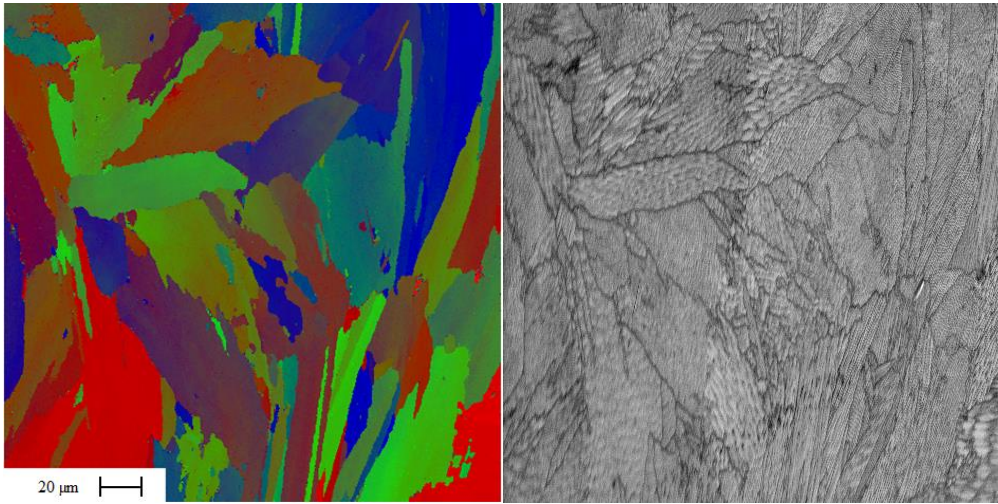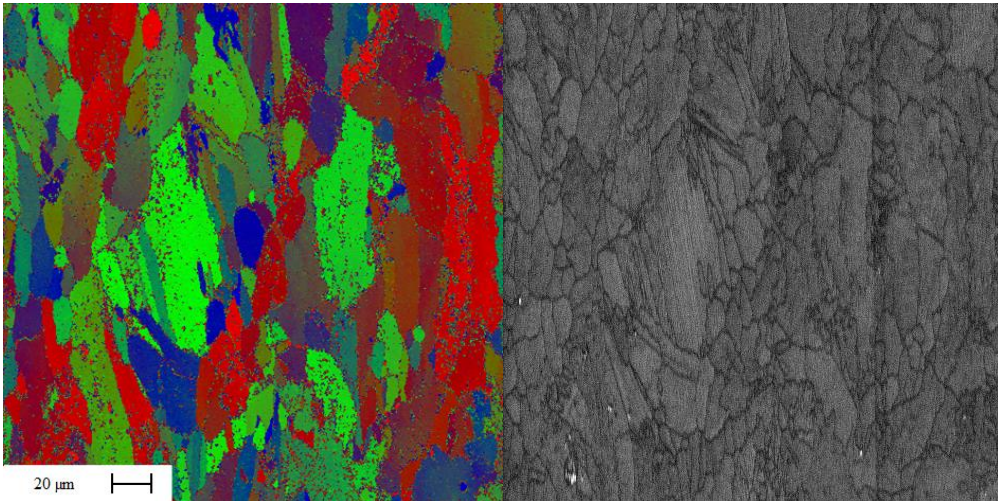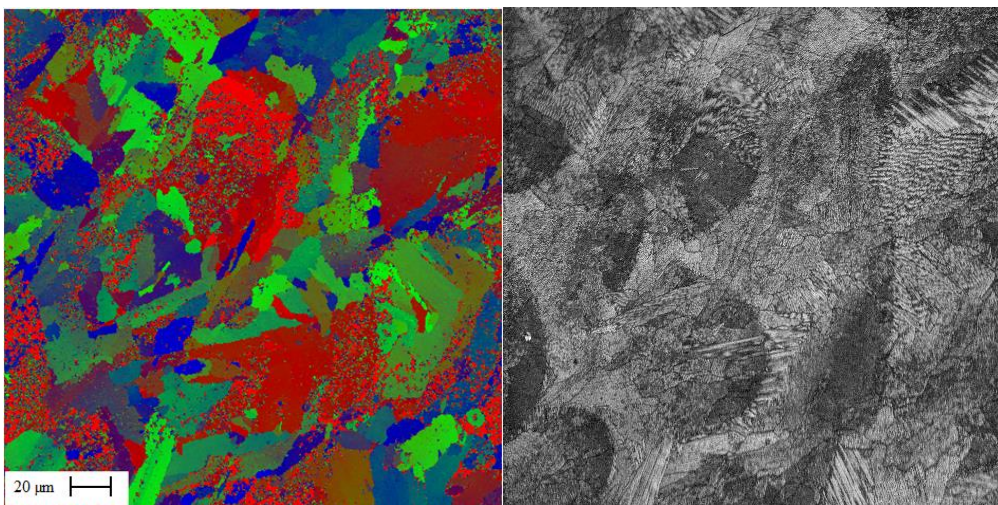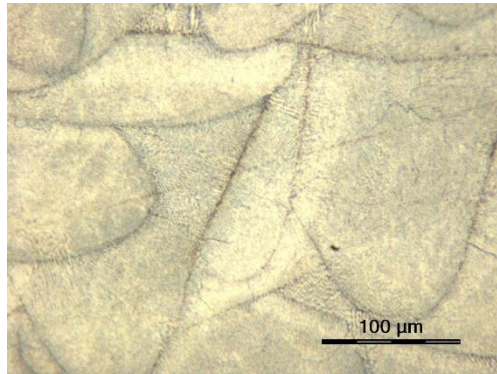*Figure 4.24: Light optical image of specimen D P. The image shows the layer structure that can be seen in the diffraction intensity image of the same specimen.*

All specimens shows colors in the entire spectrum green, blue and red. Figure 4.21 shows that green and blue are the dominant colors and red is minor in specimen H P. However, many grains have blurry colors, often reddish. Grains are generally stretched out and larger in size than grains in specimen V P and D P. Grains tend to stretch in the vertical direction of the image. Long shaped grains seem to point in the same direction as the dendrites.

Figure 4.22 shows that green seem to be the dominant color in specimen V P. Blue and red seem to be the minor colors and seem to be about evenly distributed. Some grains have blurry colors. Red spots are randomly spread out over the sample area, producing a little noisy image. The grains are varying in size. However, average grain size is smaller than for specimen H P. Grains are generally long, thin shaped and tend to stretch in the same direction, vertically in the image.

Specimen D P seem to be dominated by the color blue, as seen in Figure 4.23. Red seem to be the minor color. Many grains have blurry colors. An interesting observation is made in specimen D P. Large grains colored red fits the shape of the layers. Additionally, areas containing red dots also seem to fit the shape of the layers. This is only observed in this specimen. Figure 4.24 shows the layer structure of the specimen which can be recognized in Figure 4.23. The average grain size of specimen D P is smaller than specimen H P.

Below are images of the heat treated additive manufactured specimens presented. Figure 4.25, Figure 4.26 and Figure 4.27, shows OMs and diffraction intensity images of specimen H H, V H and D H respectively.
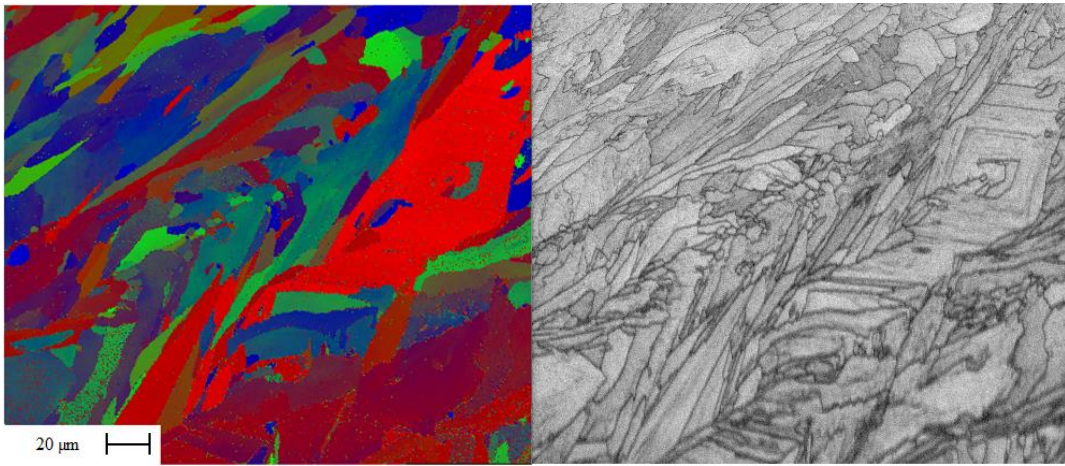
Figure 4.25: Specimen H H.
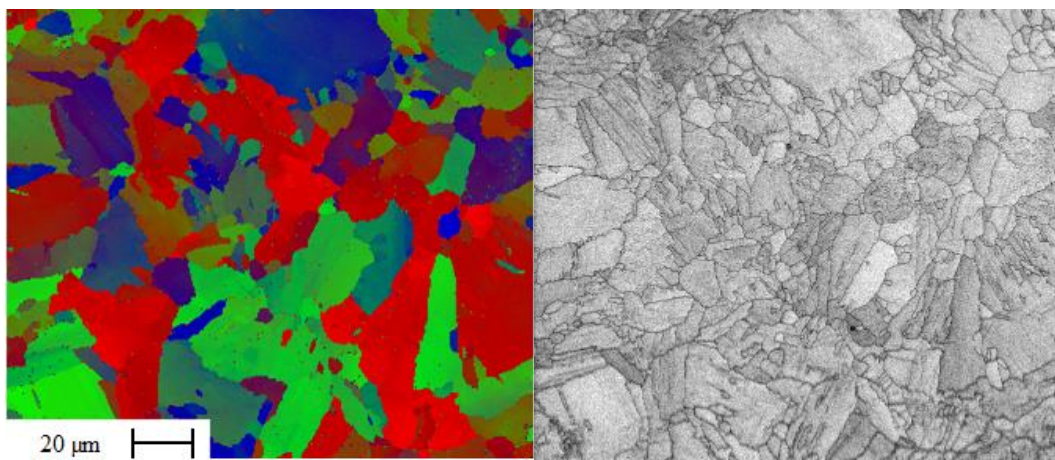
Figure 4.26: Specimen V H.
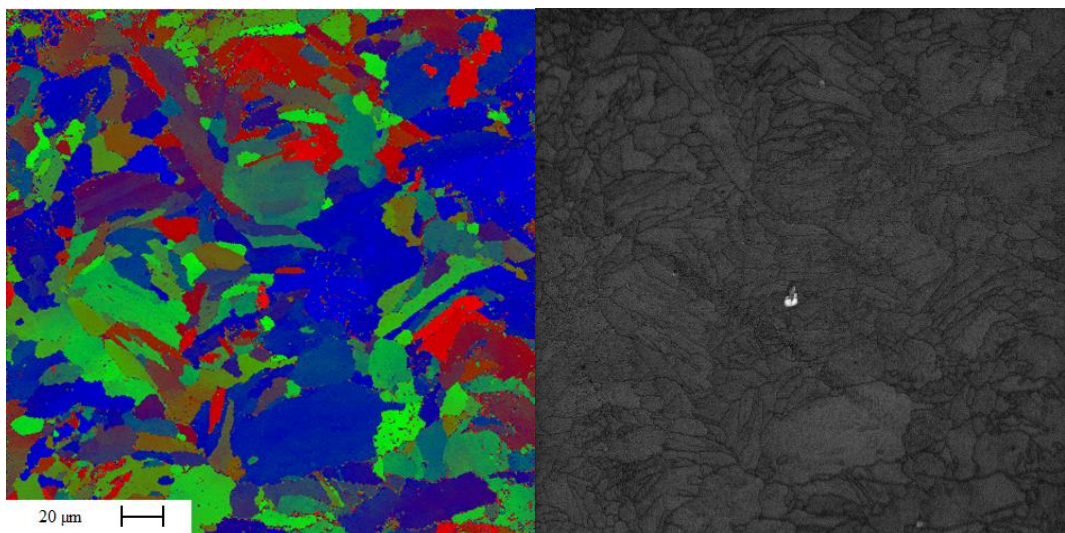
Figure 4.27: Specimen D H.

All specimens shows colors in the entire spectrum green, blue and red. Figure 4.25 shows that blue and red are the dominant colors in specimen H H and green is minor. Grains are long and thin and are stretched in the diagonal direction in the image. Many grains have blurry colors.

Figure 4.26 shows that colors of specimen V H are evenly distributed. Grains are less structured and seem less stretched and smaller than for specimen H H. Some grains have blurry colors.

Figure 4.27 shows that green and blue colors are dominant in specimen D H and red is minor. Some red spots are randomly spread out over the sample area, producing a little noisy image. Grains are less structured and seem less stretched and smaller than for specimen H H.

It is observed that H H, H P, D H and D P specimens shows signs of texture, while V P and V H shows no signs of texture.

According to [9] may the red dots observed in several specimens presented above be a result of an effect called "wraparound" effect. The effect occur when one or more angles is near a limit, causing the green, blue or red component to vary between max and min and showing color speckling where little or no actual orientation change exists.

Heat treatment was believed to make the microstructure uniform and have grain crystal orientations evenly distributed in all directions, as the forged bar specimen. However, specimen H H and D H show clear evidence of orientation in specific directions. Specimen V H however, are not orientating in specific directions. Shape of grains are varying between the three heat treated samples. Specimen H H show long thin grains, while specimen V H and D H have more rounded grains. This is somewhat a little surprising, as heat treatments were believed to make the microstructure more uniform.

5 Discussion

5.1 Influence of Texture on Tensile Properties

Tensile test results show that there are differences between the various building directions. The additive manufactured specimen in the as-printed condition which is built parallel to the pull direction of the tensile test, specimen H P, shows higher yield and tensile strength, while the specimen built normal to the pull direction, specimen V P, shows better ductile properties. EBSD analysis of specimen V P shows evenly distributed colors in the image. This means that grains orientate randomly with no preferred direction. It is said to have no or random texture. Specimen H P on the other hand, shows a domination of green and blue colors in the image. This means that grain orientation is directed, and it said to have texture. This specimen is the stronger in terms of yield and tensile strength and holds less ductile properties. This indicates that there may be a connection between crystallographic orientation and mechanical properties. Materials containing grains with randomly distributed crystallographic orientations (no texture) seem to provide ductile properties, while materials containing grains which tend to orientate in certain crystallographic directions (some texture) seem to provide yield and tensile properties. It is worth noting that the color distribution in the images is a visual consideration with room for error. Quantitative color distribution should have been determined in order to prove if grains are randomly oriented or not. It is also detected that color distribution appear different on paper than on the computer screen.

5.2 Influence of Grain Size on Tensile Properties

EBSD analysis of the various building directions also shows grain size differences between the x- and z-planes of the specimens. Whereas the horizontal build direction shows large grains in the x-plane, the vertical build direction on the other hand shows much smaller grains in the x-plane. The x-plane of the vertical build direction is equivalent to the z-plane of the horizontal build direction and the z-plane of the horizontal build direction is equivalent with the x-plane of the vertical build direction. This means that grains are small in the direction of the laser motion. Hence, the horizontal built specimen has small grains in the pull direction of the tensile test and the vertical built specimen has large grains in the pull direction. According to the Hall-Petch equation, grain size is connected to mechanical properties. Smaller grains strengthen materials by preventing dislocation movement and hence increase yield strength.

The strengthening of smaller grains in the pull direction are therefore believed to be the main contribution to higher yield strength of specimen H P than V P.

5.3 Preferred Grain Growth Direction

The differences in grain size of the planes shown by the EBSD analysis, indicate that grains have a preferred growth direction. Average grain size in the x-plane of specimen H P is larger than for specimen V P and D P. This indicates that the preferred growth direction is normal to the building direction, as the test surface for EBSD of specimen H P is normal to the building direction. Test surface of specimen V P is parallel to the building direction and test surface of D P is 45 degrees to the printing direction. These two show small grains compared to specimen H P.

5.4 Modulus of Elasticity

Tensile test results shows interesting features of the modulus of elasticity. The modulus of elasticity for the vertical built specimen shows a remarkable reduction as a consequence of heat treatment, as a 20% drop was found. The large variation in modulus of elasticity may be connected to texture in the material. According to theory, macroscopic behavior of polycrystalline material can be considered as homogenous and isotropic in terms of elastic deformation when the crystallographic texture is random. For textured materials, Young's modulus is influenced by each grains crystal orientation. This may be an indication of texture in the vertical build direction. However, the OM produced by EBSD analysis of the vertical build direction showed no evidence of texture in the material. The statistical data basis of all tests is not sufficient. One test sample is not sufficient and more samples should be tested in order to provide an acceptable statistical basis from which to draw conclusions. The remarkable reduction in modulus of elasticity may also be a result of size differences in test specimens, caused by the machining process of the test specimens.

5.5 Influence of Segregation on Mechanical Properties

Yield and tensile strength and hardness values of the additive manufactured specimens in the as-printed condition compared to the forged bar are low. Lack of γ'' precipitates and

formation of Laves phase could be an explanation for the low yield and tensile strength and hardness values. Lack of γ'' precipitates and formation of Laves phase are connected, as both phases relies on Nb. Laves phase is well known to be promoted at the cost of the Ni_3Nb phase by addition of Fe to Nb-bearing alloys. Laves phase is commonly present in Ni-base alloys because of strong segregation of Nb during solidification. Strong segregation of C also occur during solidification. The solidification sequence follows the $L \rightarrow \gamma$, $L \rightarrow \gamma + NbC$ and ends in the $L \rightarrow \gamma + Laves$ eutectic reaction when the liquid contains about 19.1wt% of Nb and 0.03wt% C. Content of C is minor in the alloy and the $L \rightarrow \gamma + NbC$ eutectic reaction is therefore not of great importance. However, the strong segregation may lead to areas gathering enough C to form NbC. As the C content is minor, it was ignored during quantitative analysis with the use of characteristic x-ray. The strong segregation behavior of C was unfortunately not considered and the element was therefore not measured.

5.6   Connection between Hardness and Tensile Properties

A connection between hardness and tensile properties are found. Hardness and tensile test values for the x-plane (indentation in the same direction as the pull) of the additive manufactured specimens in the as-printed condition show that there are a connection between the two properties. The horizontally built specimen is the strongest specimen of the three in terms of both hardness and tensile properties, while the vertically built specimen is the weakest of the three.

5.7   Influence of Heat Treatment on Mechanical Properties

Tensile and hardness test results shows that the heat treatment was successful in terms of hardness and yield and tensile strength. However, this was at the expense of properties associated with ductility, elongation at break and contraction at fracture. The additive manufactured specimens in the as-printed condition show ductile values almost as good as the forged bar. Heat treatments of the additive manufactured specimens have made them more brittle, providing low ductility. Hardness and yield and tensile strength values exceed those of the commercially produced material. It is believed that the increase is mainly a result of dissolution of Laves phase and precipitation of γ''. γ'' formation is promoted by Nb additions to the alloy. Its composition is Ni_3Nb and the phase is coherent with the γ matrix.

Strengthening in the Nb-bearing alloys, such as Inconel 718, is primarily obtained by γ''. The strength provided by γ'' is caused by large mismatch strains, about 3%, between the γ matrix and the precipitate. γ'' precipitates are not possible to detect by the use of SEM, since the precipitates are very small. TEM analysis of the samples should therefore have been performed in order to detect γ '' precipitates, as TEM provides higher magnification than SEM.

5.8   Response to Heat Treatment

Test values show that yield strength responded better to heat treatment than tensile strength, as yield strength values increased more than tensile strength values. It is observed that the interval between yield and tensile strength has become smaller by heat treatment. The interval of the additive manufactured specimens in the heat treated condition is much smaller than the interval of the forged bar.

Hardness values show that the solution annealing process has influenced the hardness of the additive manufactured specimens less than the forged bar. A small drop in hardness was noted for the additive manufactured specimens, while forged bar showed a decrease of more than 50%. No particular reason explaining this has been found.

5.9   Hardness Differences of Test Planes

Hardness test values for the additive manufactured specimens in the as-printed condition provide some interesting numbers of hardness differences connected to the test planes. It was expected that specimen D would have about the same average values for both the x-plane and the z-plane, as both test planes are 45 degrees to the printing plane. However, test results show that the x-plane is harder than the z-plane. X-plane for specimen V and z-plane for specimen H were expected to have about the same average values, because both test planes are parallel to the printing plane for both specimen. As for specimen D, test results shows that the x-plane is harder than the z-plane. The z-plane for specimen V and the x-plane for specimen H were also expected to be about the same, because both test planes are normal to the printing plane. As for specimen D and for the opposite test planes of specimen V and H, test results shows that the x-plane is harder than the z-plane. Average hardness values for the three building directions in the as-printed condition shows that the x-plane is harder than the

z-plane. No particular reason explaining this has been found. However, the standard deviation indicates that the material to some extent is inhomogeneous. Hardness testing in the z-plane of the heat treated specimens were not made as it was expected that the heat treatment would make the material uniform. However, this was not the case. The modulus of elasticity and tensile test values proves otherwise. OMs also show tendencies to orientate in specific crystallographic orientations. Testing of the z-plane should also have been made for the as-delivered forged bar for comparisons.

5.10 Optical Light Microscope and Etchant

Optical light microscope images of the as-printed additive manufactured specimens provide a good understanding of the printing process and the layer orientation. Small dark precipitates, believed to be Laves phase, are also revealed. Unfortunately no grain structure is revealed. The printing process is likely to be comparable to welding processes. An etchant for investigation of HAZ and weld metal should probably have been used for examination of the additive manufactured specimens in the as-printed condition.

5.11 Further Work

Hardness testing of the first few layers compared to the last layers would be interesting. The first few layers are subject to heat transfer from layers put on top of them, while the last layers are not influenced by heat transfer from layers put on top of them. Hardness as a function of layer thickness and thickness of parts would be an interesting relationship to establish. In order to do such a thing, one need to mark the sample once it is taken out of the machine.

Parameters from the printing process were not provided from the sample manufacturer. The parameters may be changed to optimize the printing process. A study by Qingbo Jia and Dongdong Gu [5] on how printing parameters affect the microstructure and mechanical properties of an Inconel 718 superalloy, shows that optimizing laser energy densities (J/m), laser powers (W) and scan speeds (mm/s) is of great importance to the microstructure and mechanical properties.

The statistical data basis of tensile tests are weak. More samples should have been tested in order to establish reliable data.

6 Conclusion

Additive manufacturing is a useful asset for rapid prototyping and manufacturing of parts with complex shape. Additive manufacturing of Inconel 718 produce useful mechanical properties. However, yield and tensile strength is considerably lower than for commercially produced material. Mechanical properties associated with ductility are almost equal to commercially produced material. Hardness tests shows that the additive manufactured material are softer than commercially produced material.

The heat treatment of the additive manufactured material made was partially successful. Tensile and yield properties in addition to hardness values exceeds those of commercially produced material, while properties associated with ductility are reduced significantly. Heat treatment parameters may not have been optimal to obtain the mechanical properties achievable for the alloy composition.

Various build directions of the additive manufactured material in the as-printed condition shows various mechanical properties. Tensile and hardness tests shows that the building direction parallel to the direction in which the specimen is pulled apart, the horizontally built specimen, is the stronger build direction in terms of yield and tensile strength and hardness. The building direction normal to the pull direction, the vertically built specimen, is the weaker build direction. However, the build direction normal to the pull direction holds ductile properties superior to the other build directions.

Grain size affects the mechanical properties of the various build directions. EBSD analysis shows that the horizontally built additive manufactured specimen in the as-printed condition has smaller grains than the vertically built specimen in the pull direction of the tensile test. The main contribution to higher yield strength of the horizontally built specimen compared to the vertically built specimen are believed to be the strengthening of smaller grains in the pull direction.

Crystallographic orientations seem to affect mechanical properties. Additive manufactured material in the as-printed condition built in the vertical direction hold grains with orientation evenly distributed in all directions, said to have no or random texture, and shows the superior ductile properties. Horizontal build direction shows grains that tend to orient in specific directions, said to have texture, and holds the superior yield and tensile strength properties.

The microstructure of the additive manufactured material is dendritic. Strong segregation of the alloying element Nb and C during solidification produce eutectic reactions. Low amounts of C makes most of the eutectic reaction to follow L → γ + Laves which contain large amounts of Nb. The solidification process terminates here, producing eutectic γ /Laves to form next to the γ dendrites. Heat treatment introduces γ'' and carbides and dissolves Laves. The additive manufactured material shows density comparable to commercially produced material. Microcracks and lack of fusion was observed only once.

The Eosint printed specimen is superior to the SLM printed specimen. This was expected, as the technical data provided by the machine manufacturers shows greater yield and tensile strength values for the Eosint machine.

7   References

[1]   J. DuPont, J. Lippold and S. Kiser, *Welding metallurgy and weldability of nickel-base alloys*. Hoboken, N.J.: Wiley, 2009, pp. 1-222.

[2]   C. Sims, 'A History of Superalloy Metallurgy for Superalloy Metallurgists', in *Superalloys 1984*, 1st ed., M. Gell, Ed. Warrendale: Metallurgical Society of AIME, 1984, pp. 403-407.

[3]   M. Donachie and S. Donachie, *Superalloys*, 2nd ed. Materials Park, OH: ASM International, 2002, pp. 1-37.

[4]   ASTM Standard F3055, 14a, Standard Specification for Additive Manufacturing Nickel Alloy (UNS N07718) with Powder Bed Fusion, ASTM International, West Conshohocken, PA, 2014, DOI: 10.1520/F3055-14A, www.astm.org.

[5]   Q. Jia and D. Gu, 'Selective laser melting additive manufacturing of Inconel 718 superalloy parts: Densification, microstructure and properties', *Journal of Alloys and Compounds*, vol. 585, pp. 713-721, 2014.

[6]   Ualberta.ca, 'CCWJ Teaching', 2015. [Online]. Available: http://www.ualberta.ca/~ccwj/teaching/microscopy/. [Accessed: 15- May- 2015].

[7]   J. Solberg and V. Hansen, *Innføring i Transmisjon Elektronmikroskopi*. Stavanger: University of Stavanger, 2014, pp. 10-14.

[8]   Wikipedia, 'Bragg's law', 2015. [Online]. Available: https://en.wikipedia.org/wiki/Bragg%27s_law#cite_note-5. [Accessed: 15- May- 2015].

[9]   T. Maitland and S. Sitzman, 'Electron Backscatter Diffraction (EBSD) Technique and Materials Characterization Examples', in *Scanning Microscopy for Nanotechnology*, 1st ed., W. Zhou and Z. Wang, Ed. New York: Springer, 2007.

[10]   Protolabs.com, 'Protomold: Design Tips for Rapid Injection Molding', 2015. [Online]. Available: http://www.protolabs.com/resources/design-tips/united-states/2015-05/default.htm. [Accessed: 14- May- 2015].

[11]   Instron.com, 'Tensile Testing - Instron', 2015. [Online]. Available: http://www.instron.com/sv-se/our-company/library/test-types/tensile-test?region=Sweden. [Accessed: 04- Apr- 2015].

[12]   Hardnesstesters.com, 'Vickers Hardness Test Method | Newage Testing Instruments', 2015. [Online]. Available: http://www.hardnesstesters.com/Applications/Vickers-Hardness-Testing.aspx. [Accessed: 04- Apr- 2015].

[13]   Spaceflight.esa.int, 'IMPRESS Education: Solidification, Dislocations', 2015. [Online]. Available: http://www.spaceflight.esa.int/impress/text/education/Solidification/Dislocations.html. [Accessed: 09- Jun- 2015].

[14]   Totalmateria.com, 'Precipitation Hardening of Aluminum Alloys :: Total Materia Article', 2015. [Online]. Available: http://www.totalmateria.com/page.aspx?ID=CheckArticle&site=ktn&NM=235. [Accessed: 09- Jun- 2015].

[15]   W. Callister and D. Rethwisch, *Materials science and engineering*, 8th ed. Hoboken, N.J.: Wiley, 2011, pp. 212-213.

[16]   M. Kamaya, 'A procedure for estimating Young's modulus of textured polycrystalline materials', *International Journal of Solids and Structures*, vol. 46, no. 13, pp. 2642-2649, 2009.

[17]   Special Metals Corporation*: 'INCONEL® Alloy 718 Product Brochure'*, Publication Number SMC-045, September, 2007.

[18]   API Standard 6A718, Specification of Nickel Base Alloy 718 (UNS N07718) for Oil and Gas Drilling and Production Equipment, American Petroleum Institute 2004.

[19]   G. Wynick and C. Boehlert, 'Use of electropolishing for enhanced metallic specimen preparation for electron backscatter diffraction analysis', *Materials Characterization*, vol. 55, no. 3, pp. 190-202, 2005.

Appendix A: EBSD Images

Images to the left: Image with the use of backscatter detector as it is seen in the SEM. Red rectangle shows area where OMs are made.

Images to the right: Pattern Quality images, providing grain structure.
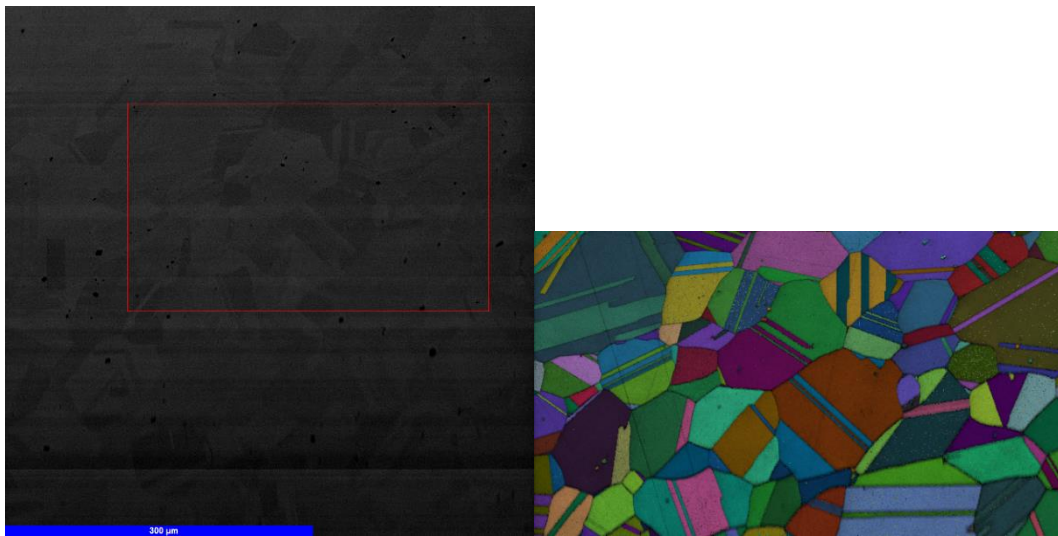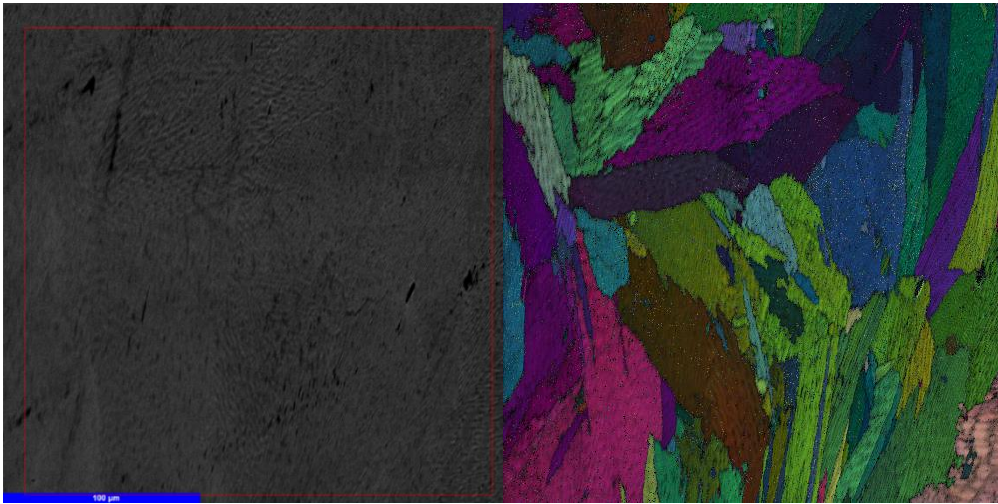

Figure A.1: Specimen FB.
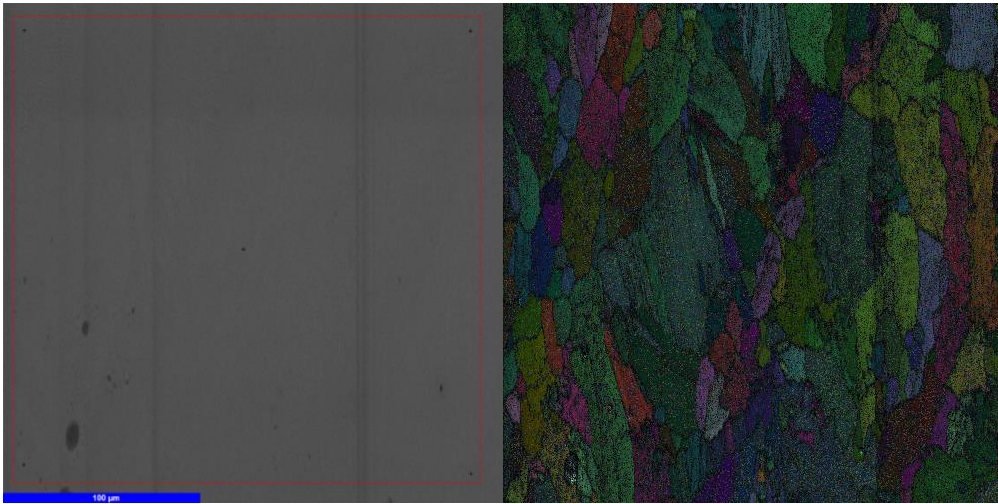
Figure A.2: Specimen H P.
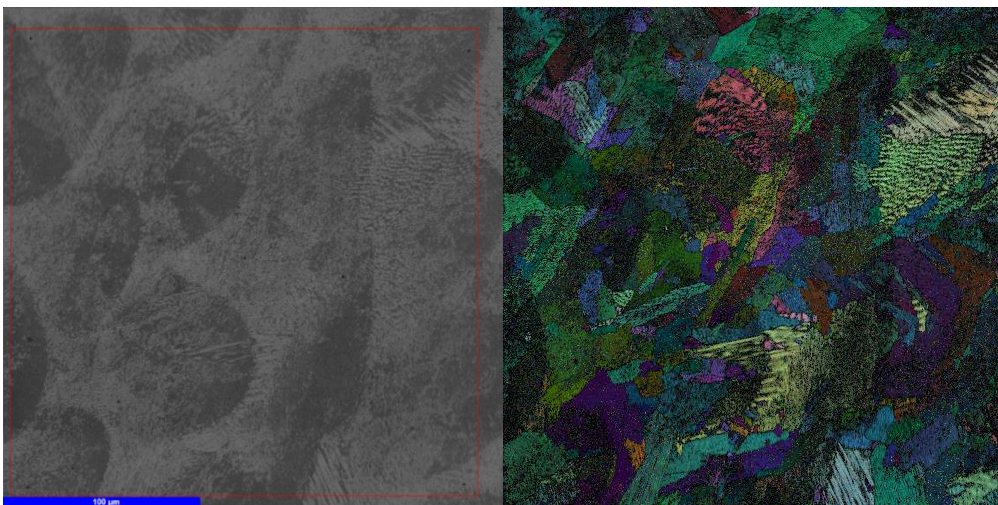

Figure A.3: Specimen V P.

Figure A.4: Specimen D P.
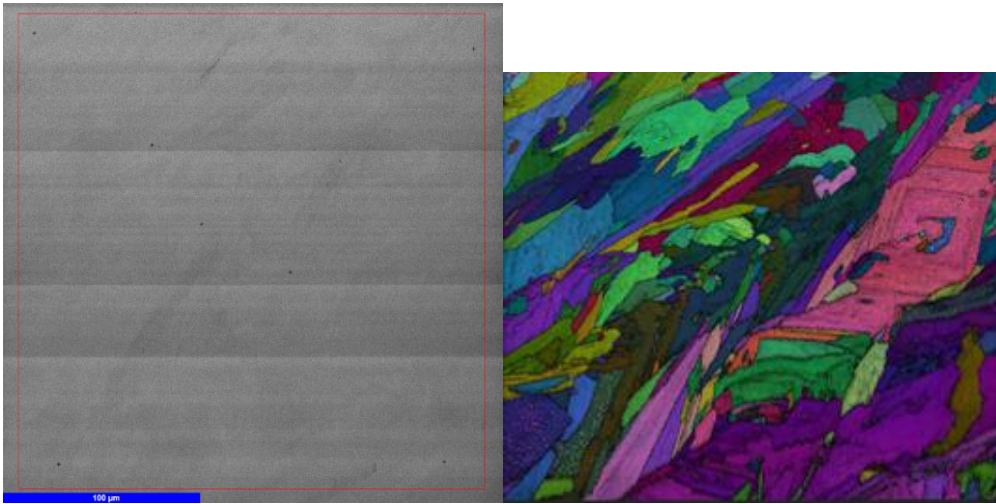
Figure A.5: Specimen H H.
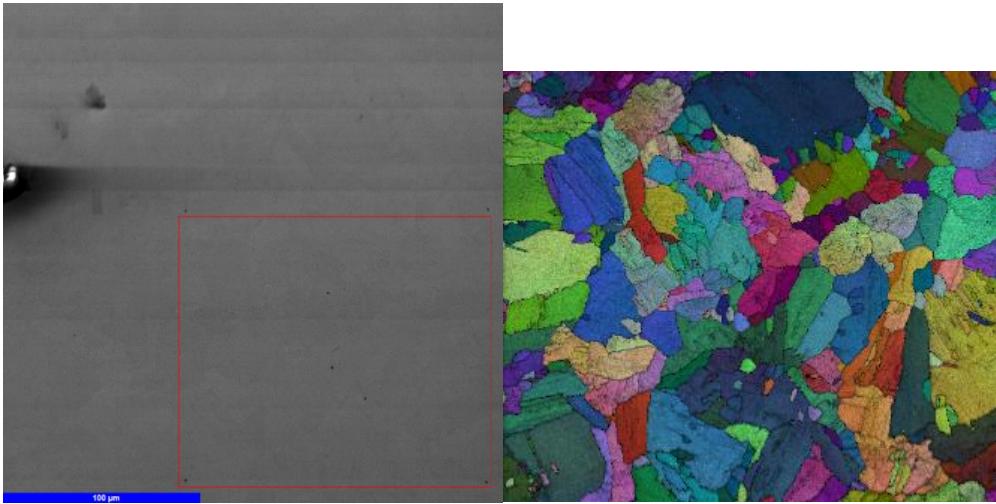
Figure A.6: Specimen V H.
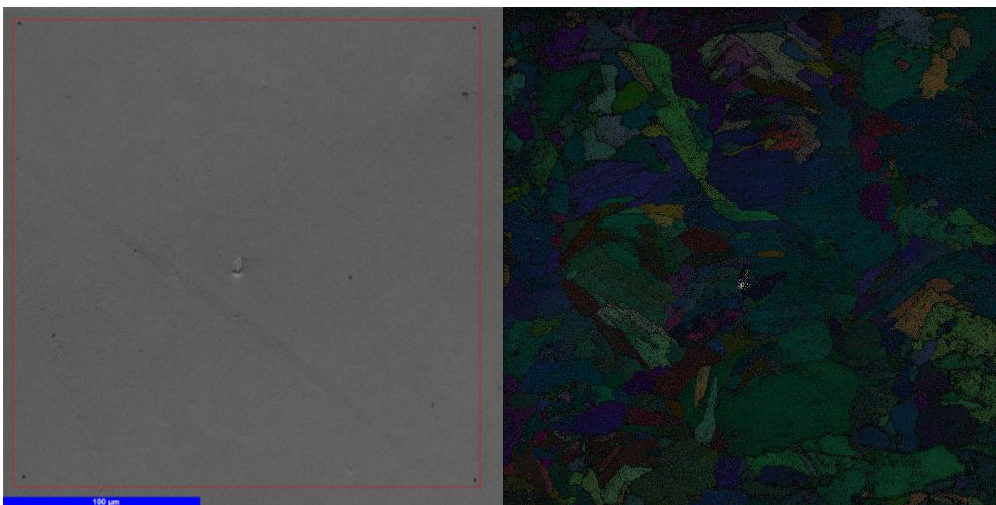
Figure A.7: Specimen D H.

Appendix B: Hardness Test Values

X-plane as-printed and as-delivered:

Table B.1: x-plane as-printed and as-delivered.

	Forged bar	V	H	D
	381	324	319	327
	379	315	322	302
	380	315	322	295
	382	298	324	305
	381	288	324	297
		319	325	301
		305	317	309
		305	304	305
Average	380.6	308.6	319.6	305.1
Standard deviation	1.1	11.9	6.9	9.9

Z-plane as-printed:

Table B.2: z-plane as-printed.

	V	H	D
	290	302	329
	305	300	296
	287	296	298
	296	293	283
	297	296	293
	301	291	288
	313	298	291
	319	295	283
Average	301.0	296.4	295.1
Standard deviation	11.0	3.6	14.7

Solution annealed:

Table B.1: Solution annealed

Forged bar	H	D
168	260	257
172	260	264
171	260	262
167	257	264
167	257	269
169	255	262
171	255	260
162	262	262
Average 168.4	258.3	262.5
Standard deviation 3.2	2.6	3.5

Age hardened:

Table B.1: Age hardened.

Forged bar	V	H	D
388	408	423	428
389	418	419	421
390	420	423	425
388	414	423	425
383	417	422	434
388	416	429	426
385	419	410	439
382	406	423	440
Average 386.6	414.8	421.5	429.8
Standard deviation 2.9	5.1	5.4	7.0

Appendix C: Typical Settings for EBSD Analysis

[NORDIF]

Software version   1.4.0

[Microscope]

Manufacturer ZEISS

Model Supra 35VP

Magnification 1000   #

Scan direction Direct

Accelerating voltage 20.0   kV

Working distance   21.6   mm

Tilt angle   70.0   °

[Signal voltages]

Minimum   0.0   V

Maximum   5.0   V

[Deflection voltages]

Minimum   -10   V

Maximum   10   V

[Electron image]

Frame rate   0.01   fps

Resolution   900x900   px

Rotation   0   °

Flip x-axis   False

Flip y-axis   False

Calibration factor   13358.8   μm/V

Tilt axis   X-axis

[Aspect ratio]

X-axis 1.000

Y-axis 1.000

[EBSD detector]

Model UF-1000

Port position   270   °

Jumbo frames False

[Detector angles]

Euler 1-   °

Euler 2-   °

Euler 3-   °

Azimuthal   -   °

Elevation   -   °

[Acquisition settings]

Frame rate   50   fps   Height 254.000 (856) µm (px)

Resolution   160x160   px   Step size   0.500   µm

Exposure time 19950 µs   Number of samples   508x499   #

Gain   8   Scan time   01:24:29

[Calibration settings]   [Points of interest]

Frame rate   8   fps

Resolution   480x480   px   [Acquisition patterns]

Exposure time 124950   µs   Acquisition (357,398)357,398   px

Gain   12   Acquisition (268,255)268,255   px

                                             Acquisition (517,484)517,484   px

[Specimen]

Name Inconel   [Calibration patterns]

Mounting   1. ND‖EB TD‖TA   Calibration (56,54)   56,54   px =>
                                             222,110,232

[Phase 1]   Calibration (847,82)   847,82 px =>
                                              242,110,260
Name Austenitt
                                             Calibration (794,825) 794,825   px =>
Pearson S.T.   -   230,110,248

IT   -   Calibration (100,830) 100,830   px =>
                                             231,103,245

 [Region of interest]

[Area]

Top   5.640 (19)   µm (px)

Left   8.015 (27)   µm (px

Width 249.500 (841) µm (px)